

El-Niño-related stratification anomalies over the continental slope off Oregon in summer 2014 and 2015

Alexander L. Kurapov¹

¹Coast Survey Development Laboratory, National Oceanic and Atmospheric Administration

December 21, 2022

Abstract

Over the continental slope off Oregon at the US West Coast, at 44.6N, vertical stratification is found to be anomalously weak in July-August of 2014 and 2015 both in a regional ocean circulation model and Conductivity-Temperature-Depth (CTD) profile observations. To understand the responsible mechanism, we focus on the layer between the isopycnal surfaces $\sigma_{\theta}=26.5$ and 26.25 kg/m³ that is found between depths 100-300 m and represents material properties characteristic of the slope poleward undercurrent and shelf-slope exchange. This layer thickness, about 50 m on average, can be twice as large during the above-mentioned periods. In the 2009-2018 model analysis, this anomaly is revealed over the continental slope only in summers 2014 and 2015 and only off the Oregon and Washington coasts (40-47N). The stratification anomaly is explained as the effect of advection of the seasonal alongslope potential vorticity (PV) gradient by an anomalously strong poleward slope current. In the annual cycle, the zone of strong alongslope PV gradient is found between 40-47N, supported by the local upwelling that results in the injection of the large PV in the bottom boundary layer over the shelf followed by its offshore transport in the slope region. The positive alongslope current anomaly propagates to Oregon with coastally trapped waves as part of the El Niño oceanic response and can be up to 0.1 m/s. Advection by this anomalous poleward current results in transporting the seasonal PV gradient earlier in the season than on average.

Abstract

Over the continental slope off Oregon at the US West Coast, at 44.6N, vertical stratification is found to be anomalously weak in July-August of 2014 and 2015 both in a regional ocean circulation model and Conductivity-Temperature-Depth (CTD) profile observations. To understand the responsible mechanism, we focus on the layer between the isopycnal surfaces $\sigma_\theta = 26.5$ and 26.25 kg m^{-3} that is found between depths 100-300 m and represents material properties characteristic of the slope poleward undercurrent and shelf-slope exchange. This layer thickness, about 50 m on average, can be twice as large during the above-mentioned periods. In the 2009-2018 model analysis, this anomaly is revealed over the continental slope only in summers 2014 and 2015 and only off the Oregon and Washington coasts (40-47N). The stratification anomaly is explained as the effect of advection of the seasonal alongslope potential vorticity (PV) gradient by an anomalously strong poleward slope current. In the annual cycle, the zone of strong alongslope PV gradient is found between 40-47N, supported by the local upwelling that results in the injection of the large PV in the bottom boundary layer over the shelf followed by its offshore transport in the slope region. The positive alongslope current anomaly propagates to Oregon with coastally trapped waves as part of the El Niño oceanic response and can be up to 0.1 m s^{-1} . Advection by this anomalous poleward current results in transporting the seasonal PV gradient earlier in the season than on average.

Plain Language Summary

Understanding the oceanic dynamics along the continental slopes is important for understanding material exchanges between the coastal and interior ocean and biological diversity. Analysis of a high-resolution, three-dimensional ocean circulation model helps explain observed variability over the slope. Associated with the global anomaly pattern called El Niño, the along-slope poleward current off Oregon was anomalously strong in summers 2014 and 2015. This anomalous transport caused alongshore displacement of the water masses from the south resulting in the vertical spreading of the subsurface oceanic layers.

1 Introduction

Seasonal ocean variability along the large part of the US West Coast, between Point Conception and Juan de Fuca Strait (Figure 1), is dominated by strong wind-driven up-

45 welling in summer and downwelling in winter (Huyer, 1983; Hickey, 1998; Austin & Barth,
46 2002; Durski et al., 2015). Upwelling supports an energetic surface intensified southward
47 coastal current, frontal instabilities, eddy generation, and jet separation that contribute
48 to the shelf-interior ocean momentum, heat and material exchange (Kosro et al., 1991;
49 Barth & Smith, 1998; Durski & Allen, 2005; Koch et al., 2010). In June-July each year,
50 a poleward undercurrent develops along the continental slope (Pierce et al., 2000; Collins
51 et al., 2013; Connolly et al., 2014; Molemaker et al., 2015). It is about 25-50 km wide
52 and its core is found between 100-300 m depths. Samelson (2017) explains the under-
53 current as part of the offshore-propagating planetary wave response following the upwelling
54 conditions setup at the coast.

55 Coastal ocean variability in this region is influenced by basin scale oceanic and at-
56 mospheric anomalies. As a recent example, one of the strongest heat waves on the record
57 hit the North-Eastern Pacific (NEP) region in 2014-2016. It was influenced by the emer-
58 gence of the "warm blob" pattern in the Gulf of Alaska early in 2014 followed by a ma-
59 jor El Niño that tried to break through early in 2014, then "fizzled" and reemerged as
60 a major event in 2015 (Bond et al., 2015; McPhaden, 2015; Rudnick et al., 2021; Amaya
61 et al., 2016; Di Lorenzo & Mantua, 2016; Jacox et al., 2016; Peterson et al., 2017; Ja-
62 ccox et al., 2019). Kurapov et al. (2022) studied impacts of this El Niño on the coastal
63 ocean dynamics along the US West Coast using a ten-year, 2009-2018, regional ocean
64 model simulation in the domain shown in Fig. 1a. Additional analyses using this model
65 are presented in this paper. The model horizontal resolution is 2 km, which allows it to
66 represent the dynamics driving shelf, slope and interior flows. The model-data compar-
67 isons demonstrate that the model reproduces correctly variability on time scales from
68 several days to seasonal and interannual. In particular, the model reproduces the El Niño
69 major features including the wide-spread warming of the surface layer, coastal sea level
70 rising, and anomalous deepening of the isopycnal surfaces over the slope (Zaba & Rud-
71 nick, 2016; Zaba et al., 2020). In summer 2014 and 2015, the flow over the shelf and slope
72 off Oregon (40-46N) can be explained as a superposition of the seasonal wind-driven up-
73 welling and the El Niño-related downwelling motion that propagates from the southern
74 boundary of the model domain as coastally trapped waves, CTW (Brink, 1991). The upwelling-
75 favorable southward winds in summers 2014 and 2015 are close to average and hence the
76 offshore near-surface transport is close to average. At the same time, the near-bottom
77 cross-shelf current exhibits an offshore anomaly (i.e., the onshore transport is weakened

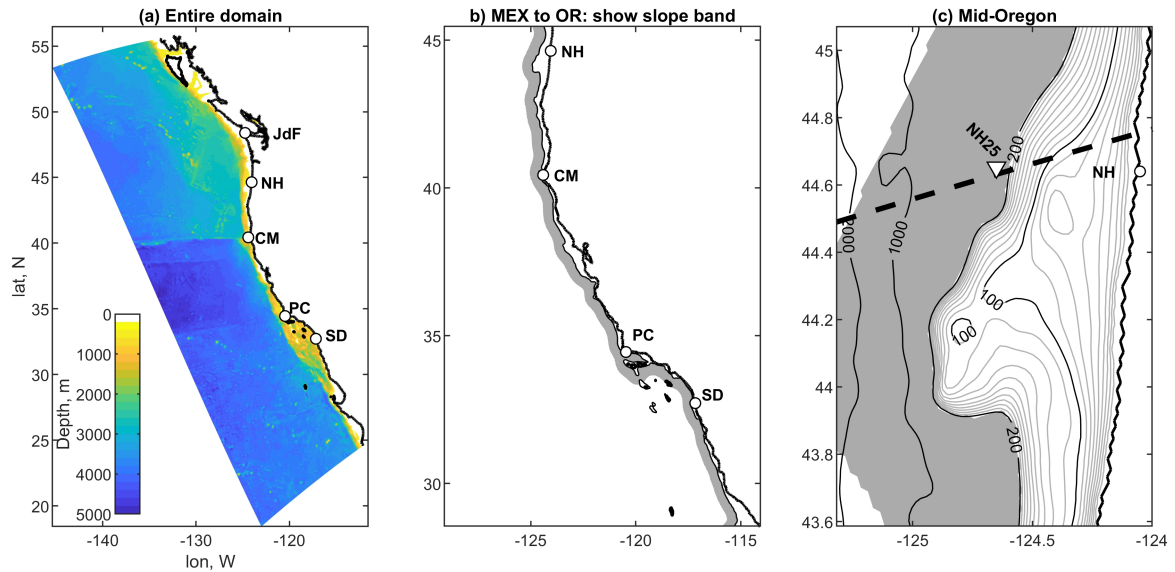


Figure 1. Maps: (a) The entire model domain, color: bathymetry; (b) a close-up on the slope area from Mexico to Oregon, to show the slope band (half-tone), defined as an area 0-40 km offshore of the 200-m isobath (black); (c) a close-up on the mid-Oregon shelf, bathymetric contours are (black) 100, 200, 1000 and 2000 m and (half-tone) from 10 to 190 m every 10 m; NH25 is the location of the ship CTD station and the dashed line is the model section (see Fig. 3 and 6); gray: the slope band. In (a)-(c), circles show geographic reference points: San Diego (SD, 32.7N), Point Conception (PC, 34.4N), Cape Mendocino (CM, 40.4N), Newport, OR (NH, 44.6N), and Juan de Fuca Strait (JdF, 48.4N).

78 or reversed toward offshore). The alongshore current component over the shelf, usually
 79 southward in Oregon, is anomalously weak. Over the slope, the poleward velocity anomaly
 80 adds to the undercurrent. This anomaly is connected to the anomalies near the south-
 81 ern boundary at 24N that propagate all along the slope with the speed of approximately
 82 2.5 m s^{-1} characteristic of CTW.

83 The 10-year model simulation at the 2-km resolution shows very rich behavior over
 84 a wide spectrum of temporal and spatial scales and provides a tool to reveal new anoma-
 85 lies and dynamical effects. In the present study, we utilize the same model solution to
 86 explain episodes of weaker stratification detected over the continental slope off Oregon
 87 in summer 2014 and 2015, both in the model and available observations. This stratifi-
 88 cation anomaly will be explained as the effect of anomalous poleward advection of the

89 seasonal alongslope gradient of the potential vorticity (PV). This will be an example where
90 a local anomaly is forced by a combination of a remote forcing (as the poleward slope
91 current anomaly propagates to the study area with CTW) and a more local, advective
92 mechanism. Explaining this effect will improve our understanding of how the shelf and
93 slope interact.

94 **2 The model and methods**

95 All the model implementation details can be found in (Kurapov et al., 2022) and
96 only a short summary is provided here. The model is based on the Regional Ocean Mod-
97 eling System, ROMS (www.myroms.org), a three-dimensional model describing the non-
98 linear evolution of the stratified ocean. The model domain (Figure 1a) extends along the
99 coast from 24N to 54N, including part of the Mexican coast, all of the US and most of
100 the British Columbia, Canada coasts. The resolution is 2 km in the horizontal and 40
101 terrain-following levels in the vertical direction. The vertical discretization is relatively
102 better near the surface and bottom such that, e.g., the top 50 m are resolved by nine or
103 more layers everywhere; over the shelf, inshore of the 200 m isobath, the bottom 20 m
104 are represented by four or more levels. The vertical coordinate z is directed upward and
105 the mean free surface is near 0; accordingly, the depths of isopycnal surfaces will be re-
106 ported below as $z_\sigma < 0$. Model atmospheric fluxes are computed using ECMWF ERA5
107 fields (ECMWF: European Center for Medium-Range Weather Forecasts, ERA: ECMWF
108 Reanalysis). Non-tidal oceanic boundary conditions are obtained from the HYCOM global
109 US Navy nowcasts (www.hycom.org). The barotropic tidal boundary conditions are added
110 using dominant harmonic constituents from the Pacific regional TPXO estimate (<https://www.tpxo.net/regional>,
111 (Egbert & Erofeeva, 2002)). The model simulation period is 1 October, 2008 – 25 Oc-
112 tober, 2018. Analyses presented below use daily averaged outputs.

113 The model does not assimilate any data inside the domain and provides a contin-
114 uous, dynamically and thermodynamically balanced solution driven only by the atmo-
115 spheric and oceanic boundary fluxes, which is most suitable for process studies.

116 Some of the analyses below are provided for the across-slope-averaged variables.
117 The approximately 40-km wide slope band is defined just offshore of the 200-m isobath
118 (shaded areas in Fig. 1b and c). This band width is chosen to be close to the width of
119 the poleward undercurrent (Pierce et al., 2000). The subsurface alongslope velocity v_s

120 is defined as in (Kurapov et al., 2022) by projecting the horizontal velocity vectors in
 121 cross-slope sections onto the alongslope direction and averaging in the horizontal across
 122 the band and in the vertical between depths of $z = -300$ and -125 m, where the core
 123 of the undercurrent is expected to be found. $v_s(y, t)$ is positive toward the north and is
 124 a function of the alongslope coordinate (precisely, the alongslope distance from the south-
 125 ern boundary) y and time t .

126 The PV is introduced in geophysical fluid dynamics as a dynamical tracer related
 127 to vorticity that is conserved following a fluid element under conditions having no dis-
 128 sipation, mixing or external boundary fluxes. In the most general form (Pedlosky, 1987):

$$PV = \boldsymbol{\omega}_a \cdot \frac{\nabla \lambda}{\rho}, \quad (1)$$

129 where $\boldsymbol{\omega}_a$ is the absolute vorticity vector and $\lambda = \lambda(p, \rho)$, a function of pressure p and
 130 density ρ , is conserved for a fluid element. If $\lambda = \sigma_\theta$ (the potential density), then the
 131 PV flux across the isopycnal surfaces is 0 even in presence of momentum dissipation and
 132 mixing in the ocean interior (Haynes & McIntyre, 1987, 1990). The PV can be injected
 133 in the layer between two isopycnal surfaces only at the atmosphere-ocean interface if the
 134 layer is outcropped (Marshall & Nurser, 1992; Thomas, 2005) or at the sloping ocean
 135 bottom (Hallberg & Rhines, 2000; Williams & Roussenov, 2003; Bethuysen & Thomas,
 136 2012; Pringle, 2022).

137 An approximation to PV adopted in this study will use only the local vertical com-
 138 ponent of the absolute vorticity (Bethuysen & Thomas, 2012):

$$q = (f + \omega)N^2 = (f + \omega) \left(-\frac{g}{\rho_0} \frac{\partial \sigma_\theta}{\partial z} \right), \quad (2)$$

139 where $\omega = \hat{z} \cdot (\nabla \times \mathbf{u})$ is the vertical component of the relative vorticity, \hat{z} the vertical
 140 unit vector, \mathbf{u} the current vector, N the buoyancy frequency, g gravity, and ρ_0 reference
 141 density. In our analyses we will present q (2) on isopycnal surfaces and in the vertical
 142 sections. While the relative vorticity is an important contributor to the PV in the vicini-
 143 ty of the slope boundary (Molemaker et al., 2015), subsurface flows away from the bound-
 144 ary are in nearly geostrophic balance, $\omega/f \ll 1$, at least on the horizontal scales resolved
 145 by our model. To estimate the cross-slope-band averaged, vertically averaged PV between
 146 two selected isopycnal surfaces, specifically $\sigma_\theta = 26.5$ and 26.25 kg m^{-3} , the background

147 PV is used that neglects ω (McDowell et al., 1982; O’Dwyer & Williams, 1997; Kurapov
148 et al., 2017b):

$$q_B = f \frac{g}{\rho_0} \frac{\Delta\sigma_\theta}{\Delta z}, \quad (3)$$

149 where $\Delta\sigma_\theta = 0.25 \text{ kg m}^{-3}$ and $\Delta z = z_{26.25} - z_{26.5}$ is the vertical distance between
150 the selected surfaces. Generally over the slope, $-300 < z_{26.5} < -175 \text{ m}$ and $z_{26.25}$ is
151 found about 50 m above $z_{26.5}$ (Kurapov et al., 2017b). So, over the slope region, the range
152 of depths between $z_{26.5}$ and $z_{26.25}$ is within the limits of -300 and -125 m used in the
153 definition of the alongslope current $v_s(y, t)$.

154 In this paper we will discuss cross-band-slope averaged variables $z_{26.5}(y, t)$, $z_{26.25}(y, t)$,
155 $q_B(y, t)$, and $v_s(y, t)$. To reduce the "noise" due to the slope eddies, a Gaussian filter with
156 the 100-km correlation length scale is applied to these functions in the y direction.

157 Time series analyses involve computation of the annual cycle and anomalies. The
158 annual cycle is defined by fitting the linear combination of the mean and three harmon-
159 ics with the periods of 1, 1/2, and 1/3 year to the time series using the pre-heat-wave
160 years 2009-2013. Kurapov et al. (2022) show that the poleward undercurrent is the salient
161 feature of the $v_s(y, t)$ annual cycle, peaking in Oregon at the end of July with the speed
162 of 0.07 m s^{-1} .

163 To provide observational evidence of episodes of the reduced stratification over the
164 slope off Oregon in the El Niño years, repeated ship CTD profile data are utilized at sta-
165 tion NH25 along the Newport Hydrographic (NH) Line (44.65N) located 25 nautical miles
166 offshore, where the total water depth is $h = 275 \text{ m}$ (Fisher et al., 2015; Peterson et al.,
167 2017; Risien et al., 2022) (Figure 1c). This unique time series, 1999 through present, is
168 a result of the multiyear effort led by W. Peterson, J. Fisher et al. attempting to main-
169 tain the two-week frequency of hydrographic and biogeochemical profile observations at
170 several stations at the NH line, although stations offshore of $h = 200 \text{ m}$ were visited
171 less often.

172 **3 The stratification anomaly over the slope**

173 We have already shown that $z_{26.5}$ over the slope off Oregon is anomalously deep
174 in 2014-2015 (Kurapov et al., 2022). New analyses focus on the anomalies in both $z_{26.5}$

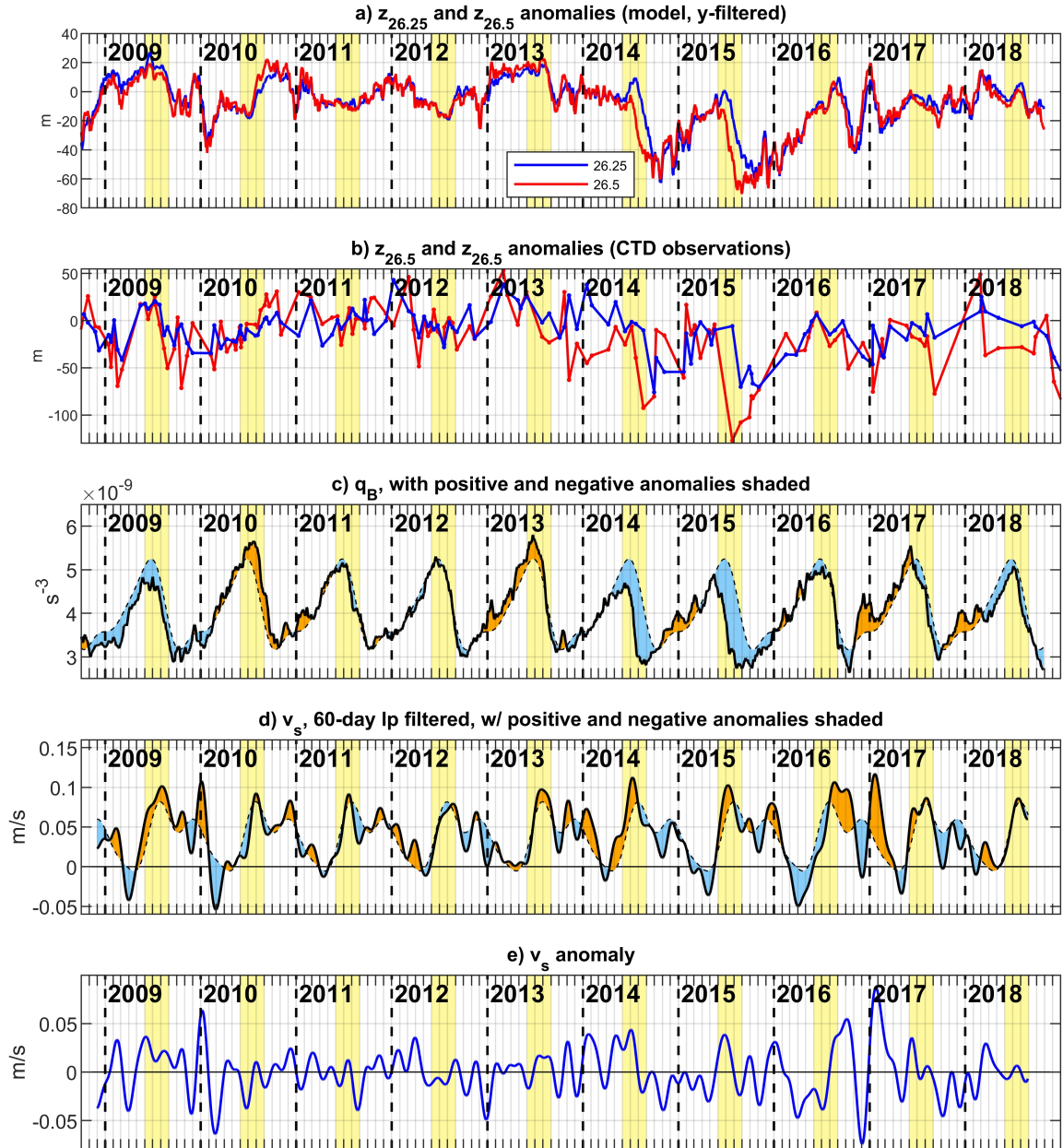


Figure 2. Time series at 44.6N: (a) model $z_{26.5}$ and $z_{26.25}$ anomalies averaged across the slope band (i.e., 0-40 km offshore of the 200-m isobath); (b) observed $z_{26.5}$ and $z_{26.25}$ anomalies, ship CTD at the NH25 station ($h = 275$ m), (c) solid line: model q_B averaged across the slope band, dashed line: annual cycle in q_B ; (d) solid line: v_s , dashed line: annual cycle in v_s ; (e) v_s anomaly. The anomalies are with respect to the annual cycle, based on 2009-2013. In (c) and (d), the orange and blue shades show positive and negative anomalies from the annual cycle. Vertical dashed lines: 1 January of each year. Yellow shades: summer months (JJA). Tick marks on the time axis are on the 1st of each month.

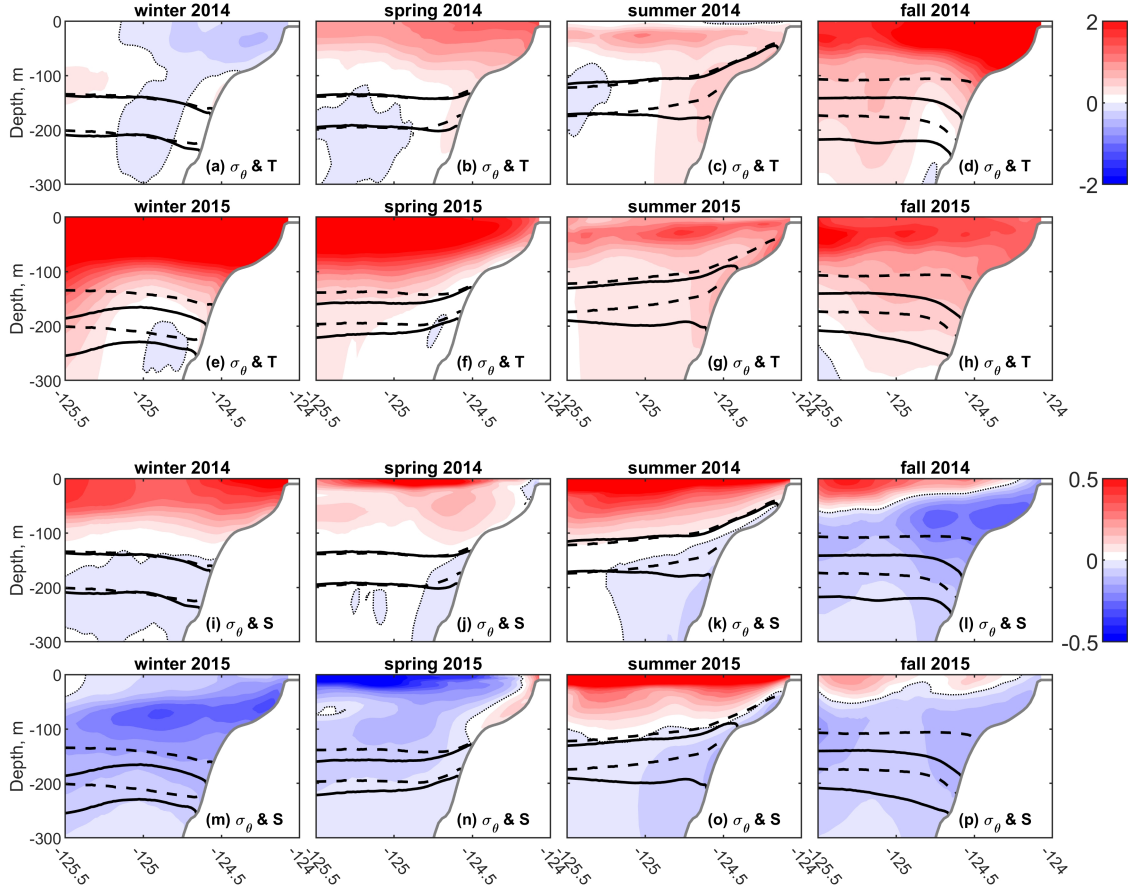


Figure 3. Black thick contours: the seasonally averaged $\sigma_\theta = 26.5$ and 26.25 kg m^{-3} in 2014-2015 in the model cross-shore section near the NH line, 44.6N (see Fig. 1c for the section location): (solid) 3-month averages in 2014 and 2015, (dashed) 2009-2013 average for each season. Background color: seasonal anomalies in (rows 1-2) T ($^\circ\text{C}$), (rows 3-4) S . Winter, spring, summer and fall are defined as DJF, MAM, JJA, and SON, correspondingly. The thin dotted contour shows T or S zero anomaly.

175 and $z_{26.25}$, averaged across the slope band (Figure 2a). These vary in unison (*i.e.*, Δz
 176 anomaly is near 0) for most of the 10-year study period. The notable exceptions are two
 177 periods, July-August of each 2014 and 2015, when not only the depth of each
 178 surface is the deepest, but also Δz is increased by about 50 m. In the NH25 CTD pro-
 179 file data (Fig. 2b), the separation between these layers is also anomalously large during
 180 the same time periods. In 2015, the observed local Δz anomaly is in excess of 100 m.

181 Over the slope off Oregon, q_B averaged between $z_{26.5}$ and $z_{26.25}$ shows a strong up-
 182 welling/downwelling annual cycle (Fig. 2c). The strongest negative anomalies are pre-
 183 sented in summer of each 2014 and 2015, consistent with the strong Δz anomalies dur-
 184 ing the same period. Figure 3 presents this anomaly in a model cross-shore vertical sec-
 185 tion near the NH line (the section location is shown in Fig. 1c). In these section plots,
 186 the thick black contours show 3-month averaged σ_θ in 2014 and 2015 (solid lines) and
 187 seasonal climatological σ_θ (dashed lines). The background color is the seasonal T (rows
 188 1,2) or S anomalies (rows 3,4). Both isopycnal surfaces, 26.25 and 26.5 kg m^{-3} , are near
 189 their climatological levels in winter and spring 2014 (Figure 3a,b,i,j). In summer 2014
 190 (c,k), $z_{26.25}$ is near the climatological level supported by the upwelling favorable winds.
 191 At the same time, $z_{26.5}$ is depressed resulting in the weaker stratification anomaly over
 192 the slope. In fall 2014 (d,l), both isopycnal surfaces are about 50 m below their clima-
 193 tological levels, but the relative distance Δz is again close to the climatology. In win-
 194 ter 2015 (e,m), the isopycnal surfaces are still depressed relative to climatology. By spring
 195 2015 (f,n), these are moved up over the slope by upwelling reaching the climatological
 196 levels over the shelf. Summer 2015 (g,o) is similar to summer 2014 showing the anoma-
 197 lously large spreading between the layers over the slope, mainly due to $z_{26.5}$ anomalous
 198 deepening.

199 In a series of plots in Figure 3a-h, it may be noticed that the $z_{26.5}$ anomaly near
 200 the slope leads the anomaly at the offshore extent of the cross-section shown. This ef-
 201 fect can be associated with the offshore planetary wave propagation (Kurapov et al., 2022).

202 The near-bottom T anomaly over the shelf and slope in summers 2014 and 2015
 203 (Fig. 3c,g) is accompanied by the fresher S anomaly (k,o) and is a signature of the El
 204 Niño-related downwelling. The extreme T anomaly, in excess of 2°C , shows in the top
 205 100 m in fall 2014 (Fig. 3d) after the warm blob waters reach the shelf (Barth et al., 2018).
 206 The strong S anomaly extending over the shelf and slope is evident starting fall 2014.
 207 This and other details of the T and S anomalies are intriguing but require more detailed
 208 analyses and are left as a topic of future studies.

209 To see where along the slope the q_B anomalies reveal themselves and how they may
 210 compare to v_s , the anomalies in $v_s(y, t)$ and $q_B(y, t)$ are shown as Hovmöller diagrams.
 211 Anomalies in v_s (Figure 4a) exhibit fast propagating CTW patterns as discussed in (Kurapov
 212 et al., 2022). In spring-summer 2014 and summer 2015 episodes of sustained positive anoma-

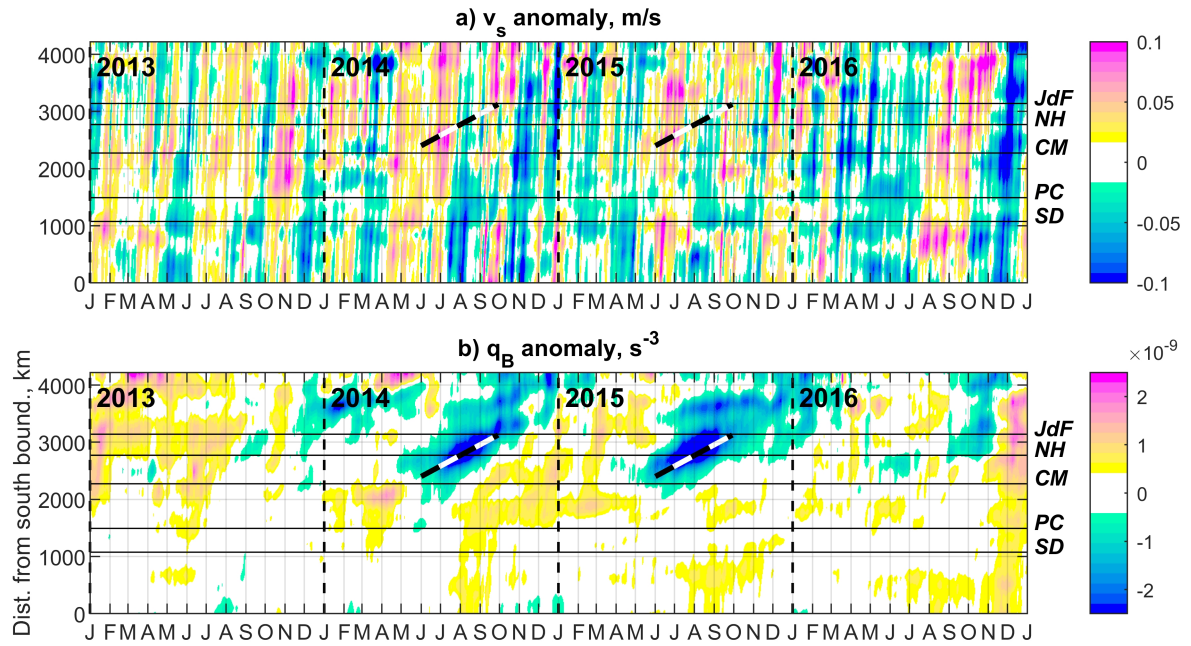


Figure 4. Time vs. alongslope distance plots of anomalies in the slope-band averaged properties, 2013-2016: (a) v_s , (b) q_B . The dashed guidelines correspond to the characteristic advective speed of 0.07 m s^{-1} . Vertical dashed lines show 1 January of each year. Horizontal lines show reference coastal points (see Fig. 1): San Diego (SD, 32.7N), Point Conception (PC, 34.4N), Cape Mendocino (CM, 40.4N), Newport, OR (NH, 44.6N), and Juan de Fuca Strait (JdF, 48.4N).

213 lies reaching 0.1 m s^{-1} are evident, connected to the model southern boundary. In con-
 214 trast, the q_B diagram (Figure 4b) does not show the strong CTW signal. The negative
 215 anomalies of 2014 and 2015 are found only north of Cape Mendocino (CM, 40.4N) in North-
 216 ern California and are the largest between CM and Juan de Fuca Strait (JdF, 48.4N),
 217 i.e. along the coasts of Oregon and Washington. In each summer, the anomalies emerge
 218 just north of CM coinciding with the time of the large positive v_s anomaly. Then the
 219 negative disturbance is transported northward with the speed of 0.07 m s^{-1} character-
 220 istic of the poleward undercurrent.

221 Our hypothesis is that the advection of the alongslope gradient of q by the anoma-
 222 lously strong v_s drives the summer 2014 and 2015 q_B anomalies. In the symbolic form,
 223 the dominant balance is as follows:

$$\frac{\partial q_B}{\partial t} \approx -v_s \frac{\partial q_B}{\partial y}. \quad (4)$$

224 This balance will be tested below (section 5). We already noted in the introduction that
 225 v_s was anomalously strong during those periods. The time series of the total v_s , its an-
 226 nual cycle, and the anomaly at the NH latitude (Figure 2d,e) show that although the
 227 anomalies are not standing out as uniquely large in summer 2014 and 2015, they turn
 228 out to be the largest among all the summers. It is possible that not only the anomaly
 229 magnitude is important but also its longevity and timing relative to the peak of v_s in
 230 the annual cycle. Given the relatively modest speeds at the level of the undercurrent,
 231 to make the alongslope advection in the isopycnal layer a significant contributor to the
 232 tendency in q_B (4), the anomaly in v_s must be accompanied by the strong enough $\partial q_B/\partial y$.

233 4 The seasonal alongslope PV gradient

234 The annual cycle in $q_B(y, t)$ (Figure 5) does indeed show a zone of strong $\partial q_B/\partial y$
 235 that undulates between CM in summer and an area north of JdF in winter. q_B increases
 236 sharply and almost simultaneously in the area between CM-JdF in April, coinciding with
 237 the beginning of the upwelling season. With the onset of the undercurrent in June-July,
 238 the zone of the large gradient starts drifting from CM to JdF with the speed of a few
 239 cm s^{-1} . Notably, the large seasonal gradient $\partial q_B/\partial y$ is found in the same area where
 240 q_B anomalies are detected in 2014 and 2015.

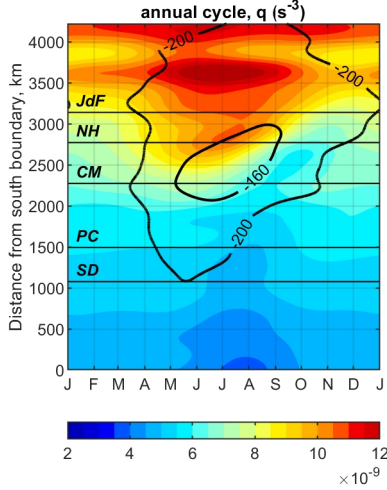


Figure 5. The annual cycle in $q_B(y)$. Black contours: annual cycle in $z_{26.5} = -200, -160$ m. Horizontal lines show reference coastal points (see Fig. 1): San Diego (SD, 32.7N), Point Conception (PC, 34.4N), Cape Mendocino (CM, 40.4N), Newport, OR (NH, 44.6N), and Juan de Fuca Strait (JdF, 48.4N).

241 The reason for the sharply higher q_B in the area of strong upwelling in summers
 242 is found to be due to the PV injection in the bottom boundary layer (BBL) over the slop-
 243 ing shelf bottom (Bethuysen & Thomas, 2012) followed by the PV anomaly entrainment
 244 from the shelf BBL to the interior layer over the slope. Physically, the PV injection across
 245 the sloping bottom during upwelling can be explained first as the geometric effect of the
 246 increase in N the near bottom. Second, the strong tendency toward BBL arrest takes
 247 place (MacCready & Rhines, 1991, 1993; Garrett et al., 1993). As part of this process
 248 the horizontal density gradient established in the BBL due to upwelling is balanced by
 249 the vertical shear in the alongshore velocity component such that the alongshore cur-
 250 rent is reduced near the bottom. As a result, the cross-shore horizontal velocity gradi-
 251 ent is established between points in the BBL and points above the BBL farther offshore
 252 such that $\omega > 0$ near the bottom. So, both N and ω contribute to the increase in q (2)
 253 in the BBL over the sloping bottom.

254 To illustrate that our model represents this process, q is shown together with the
 255 the daily averaged alongslope velocity in the NH cross-shore section (Figure 6). For ex-
 256 ample, on March 31, 2011 (Fig. 6a,c), before the onset of the first upwelling event of the

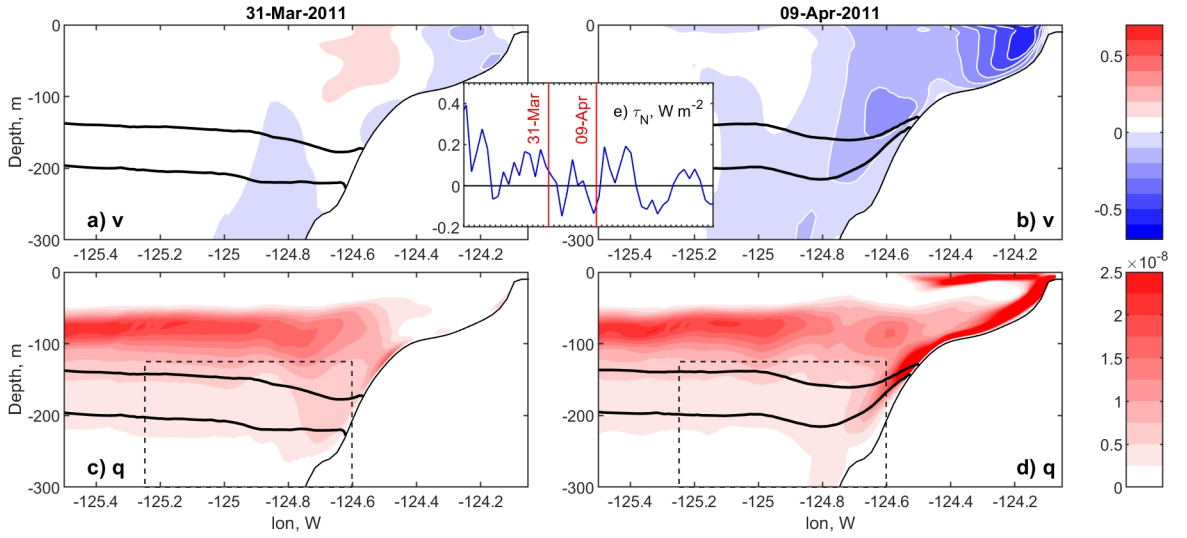


Figure 6. Cross-shore sections near the NH line of daily-averaged (TOP) meridional velocity component, m s^{-1} , (BOTTOM) potential vorticity q , s^{-3} ; (LEFT) 31 March 2011, before the first upwelling event of the year, (RIGHT) 9 April 2011, following the peak of the upwelling event. Black contours are $\sigma_\theta = 26.25$ and 26.5 kg m^{-3} . In (c)-(d), the dashed box is the slope area where v_s average is defined. (e) Daily-averaged meridional wind stress component (northward is positive) between 15 March - 1 May 2011, with red lines showing the dates selected for the cross-section plots.

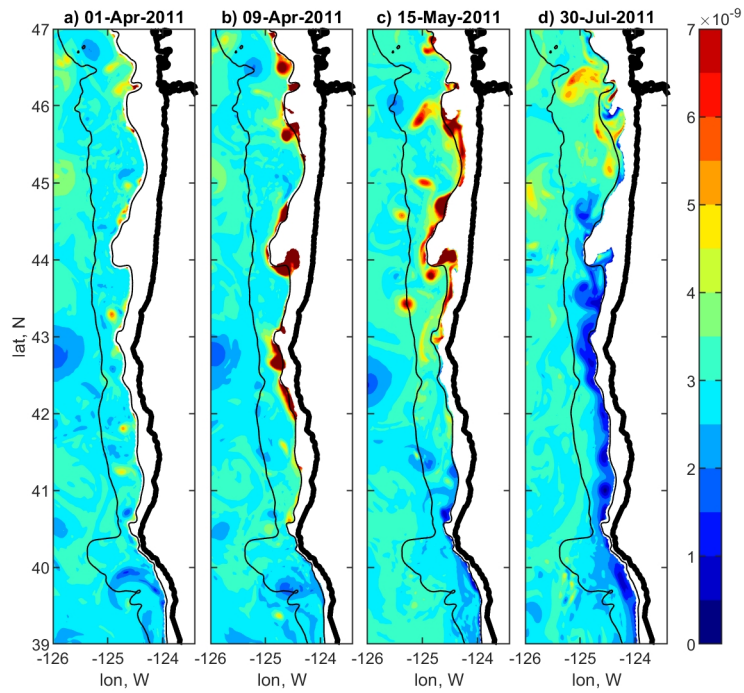


Figure 7. Maps of daily-averaged q (s^{-3}) on the isopycnal surface $\sigma_\theta = 26.5 \text{ kg m}^{-3}$ in the coastal area including Northern CA, all of Oregon and part of Washington State. Black contours are isobaths (200 and 2000 m).

257 year, the alongshelf current is low. At this time, q is relatively large in the interior at
 258 the depth of the winter pycnocline and is low over the shelf. With the onset of upwelling,
 259 as on April 9, 2011 (Fig. 6b,d), q is large over the shelf. In this example, a tongue of high
 260 q is seen in the layer between the surfaces $\sigma_\theta = 26.25$ and 26.5 kg m^{-3} that will be trans-
 261 ported later within that layer to the area over the slope. Maps of the daily-averaged q
 262 computed on $z_{26.5}$ (Figure 7) show relatively low q over the slope before the upwelling
 263 starts (Fig. 7a), followed by episodes of higher q transported with eddies from the shelf
 264 to the slope area following a series of upwelling events (b, c). The emerging undercur-
 265 rent (c,d) is associated with the low q anomaly supported by the negative ω near the slop-
 266 ing bottom (Molemaker et al., 2015). Where the upwelling-related high and undercurrent-
 267 related low q meet, the largest $\partial q/\partial y$ is found. As the season progresses, the undercur-
 268 rent "flushes" the slope waters in Oregon-Washington, pushing the high gradient area
 269 farther and farther north. Note that $\omega < -f$ is a condition for the onset of centrif-
 270 ugal instability (Haine & Marshall, 1998), such that $q > 0$ in Figure 7.

271 Pelland et al. (2013) studied coastal undercurrent eddies, or "cuddies" using glider
 272 hydrographic transects off the coast of Washington. They find that about one third of
 273 the cuddies detected in the ocean interior are anticyclonic and are associated with the
 274 patches of positive PV anomaly. Our model reproduces eddies similar to those anticy-
 275 clonic cuddies (see Fig. 7). The relatively higher PV in these eddies is evidently of the
 276 shelf origin.

277 **5 Term balance analysis for q_B**

278 In this section it will be demonstrated that despite all the approximations that go
 279 into (4), it describes very well the seasonal evolution of the slope averaged q_B as well as
 280 the 2014 and 2015 summer anomalies. To summarize, the approximations include: (i)
 281 ω is neglected; (ii) q_B is the average PV in an area bounded by the two selected isopy-
 282 cnal surfaces and the horizontal extent of the slope band; (iii) v_s is used as the advec-
 283 tive velocity, which is an average in a larger area that includes the selected isopycnal layer
 284 (see the dashed rectangle in Figure 6); (iv) the q flux from the shelf and the slope bot-
 285 tom and the offshore flux are ignored; (v) the alongshore filter is applied to both $v_s(y, t)$
 286 and $q_B(y, t)$; (vi) daily-averaged values are utilized in the model that resolves the tides.
 287 In Figure 8, $TEND = \partial q_B/\partial t$ (half-tone) is compared to $ADV = -v_s \partial q_B/\partial y$ (red) at
 288 the NH latitude; the annual cycle in ADV (blue) is added for reference. $TEND$ is rather

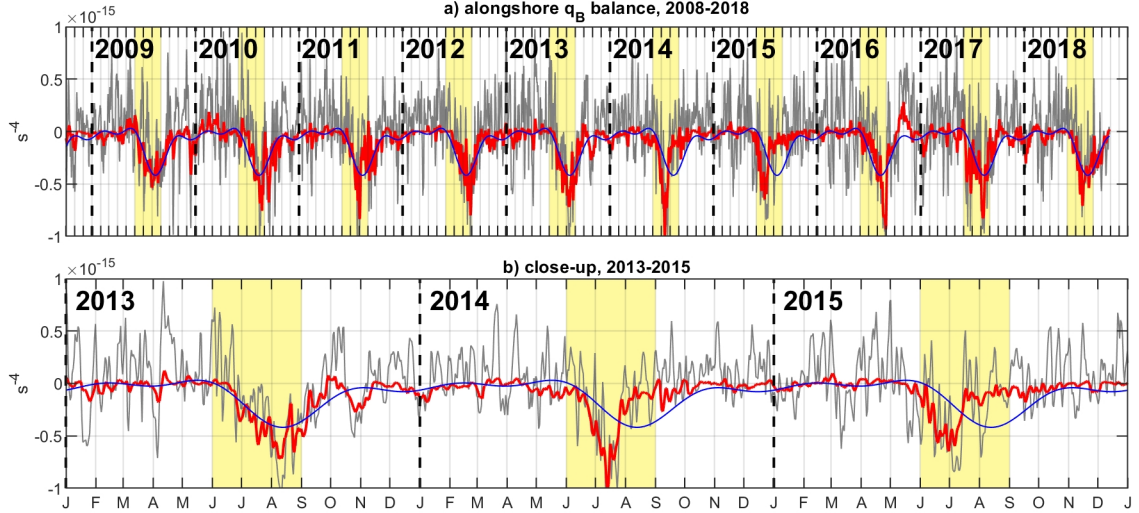


Figure 8. The PV term balance analysis over the slope at NH line: (gray) tendency $\partial q_B / \partial t$, (red) $ADV = -v_s \partial q_B / \partial y$, (blue) annual cycle in ADV (based on 2009-2013). (a) the entire 2008-2018 time period, (b) focus on 2013-2015. Vertical dashed lines: 1 January of each year. Yellow shades: summer months (JJA).

289 noisy as it is estimated from the daily values, but the drop to the strongly negative val-
 290 ues is apparent every summer, associated with the passage of the high $\partial q_B / \partial y$ zone and
 291 the trail of the low q_B in the undercurrent. This pattern is followed very closely by ADV .
 292 In a close-up on 2013-2015 (Figure 8b), it is particularly clear that variability in 2013
 293 is near average, which will be a staple of every year except 2014 and 2015. In those two
 294 years, ADV decreases and recovers about one or two months earlier than on average and
 295 $TEND$ follows the same pattern. It is not necessarily the stronger negative ADV but the
 296 earlier onset of the transition period that makes q_B anomalous in 2014 and 2015.

297 Next, each q_B and v_s can be written as a sum of the annual cycle and anomaly:
 298 $q_B = Q_B + q'_B$ and $v_s = V_s + v'_s$. At the NH location, it is confirmed that $\partial Q_B / \partial t$
 299 closely follows $-V_s \partial Q_B / \partial y$ (not shown). Then,

$$\frac{\partial q'_B}{\partial t} \approx -V_s \frac{\partial q'_B}{\partial y} - v'_s \frac{\partial Q_B}{\partial y} - v'_s \frac{\partial q'_B}{\partial y}. \quad (5)$$

300 The narrative offered so far, that "the slope current anomaly carries the seasonal PV along-
 301 shore gradient" may suggest that the tendency on the lhs of (5) is mostly controlled by

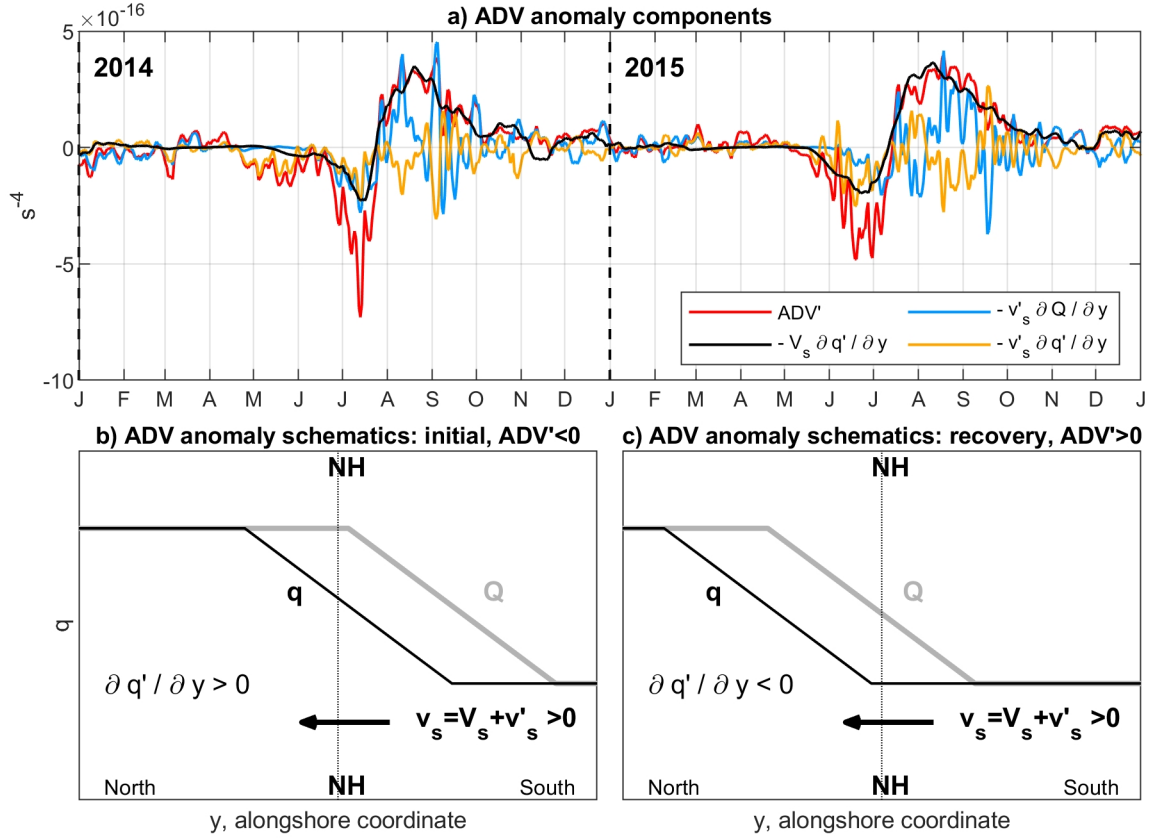


Figure 9. (a) Time series (2014-2015) of the (red) ADV' anomaly and its contributing terms: (black) $-V_s \partial q' / \partial y$, (light blue) $-v'_s \partial Q / \partial y$, (orange) $-v'_s \partial q' / \partial y$; (b-c) schemes explaining the sign of each of the contributing terms to the ADV' anomaly. At the initial phase, all the three contributing terms are negative. At the recovery phase, $\partial q / \partial y$ is small, thus $-v'_s \partial Q / \partial y$ and $-v'_s \partial q' / \partial y$ nearly balance each other.

302 the second term on the rhs. However, this is not the case (Figure 9a). In summer 2014
 303 and 2015, the sum of the all the terms on the rhs of (5), ADV' , goes first through the
 304 initial, negative phase followed by the positive recovery phase. At the initial phase all
 305 the three terms contribute equally to ADV' . At the recovery phase, term $-V_s \partial q'_B / \partial y$
 306 follows closely ADV' and the other two terms on the rhs of (5) nearly balance each other.
 307 This behavior fully supports the assertion that the PV anomalies are caused by the ear-
 308 lier than usual advection of the strong PV front by the anomalously strong current. At
 309 the initial phase (Figure 9b), the zone of the strongest $\partial q / \partial y$ moves through section NH
 310 early, while $\partial Q / \partial y \approx 0$. Hence $\partial q' / \partial y > 0$ and the term $-v'_s \partial q'_B / \partial y$ initiates the neg-
 311 ative anomaly in ADV' . The other two terms will eventually contribute, too, when V_s
 312 and $\partial Q / \partial y$ reach seasonal peaks. At the recovery phase, after the front has passed, $\partial q / \partial y =$
 313 $\partial Q / \partial y + \partial q' / \partial y \approx 0$ such that $-v'_s \partial Q_B / \partial y$ and $-v'_s \partial q'_B / \partial y$ nearly balance each other.

314 6 Concluding remarks

315 The regional ocean circulation model helps to discover and explain the events of
 316 anomalous stratification weakening in a layer over the slope off Oregon in July-August
 317 2014 and 2015. The alongslope advection of the strong seasonal PV gradient earlier in
 318 the season than usual explains the PV tendency anomaly and hence the stratification
 319 anomaly. This anomaly is triggered by the anomalously strong (by as much as 0.1 m s^{-1})
 320 and persistent alongslope current anomaly that arrives on the Oregon slope with the coastally
 321 trapped waves originating at the southern boundary and triggered by the El Niño oceanic
 322 mechanism.

323 As part of this study we also evaluated, but could not confirm, if the cross-shore
 324 PV flux anomalies also contribute to the stratification anomalies studied. The expect-
 325 ation was that the downwelling motion associated with the El Niño may provide an ad-
 326 ditional local source of negative PV anomaly over the slope. The downwelling is asso-
 327 ciated with the PV destruction over the slope (Bethuysen & Thomas, 2012) due to the
 328 geometric effect of the weakened stratification near the bottom. Enhanced mixing in-
 329 cluding convective instability (Moum et al., 2004) may also contribute to PV destruc-
 330 tion during downwelling. There is also a possibility that the negative cross-shore veloc-
 331 ity anomaly fluxes this PV deficit into the slope area. However, our analyses of the q flux
 332 across the 200-m isobath at the NH section (not shown) did not exhibit any strikingly
 333 anomalous behavior in the range of depths between $z_{26.5}$ and $z_{26.25}$ in summer 2014 or

2015. Two facts additionally point to the alongslope advection as the dominant mechanism explaining the stratification anomalies: (i) the q_B anomaly is found only where the seasonal $\partial Q/\partial y$ is large, and (ii) this anomaly, first appearing near Cape Mendocino in the Northern CA is displaced to the north with the speed characteristic of the poleward undercurrent.

While surface oceanic processes are well sampled by satellite sensors, subsurface flows remain undersampled. Availability of long-time continuous in-situ observational time series, similar to the CTD set used here, is very important for assessing dynamical processes on intraseasonal, seasonal, and interannual temporal scales. Accurate high-resolution models that show variability consistent with the sparse in-situ data remain important instruments to improve our understanding of subsurface flows, including in our case processes that define the shelf-interior ocean material and heat exchange.

Acknowledgments

We wish to thank Drs. K. Brink, P. MacCready, I. Rivin and J. Pringle for useful discussions. We are grateful to Jennifer Fisher for providing the CTD profile data. This research was partly supported by the NASA grant 80NSSC22K1003.

Data Availability Statement

CTD observations utilized in this study are available as described in (Risien et al., 2022). Model outputs and the entire model setup are freely available upon request to anybody interested in future analyses or developments.

References

- Amaya, D. J., Bond, N. E., Miller, A. J., , & DeFlorio, M. J. (2016). The evolution and known atmospheric forcing mechanisms behind the 2013-2015 north pacific warm anomalies. *US Clivar Var.*, *14*, 1-6.
- Austin, J. A., & Barth, J. A. (2002). Drifter behavior on the Oregon–Washington shelf during downwelling-favorable winds. *J. Phys. Oceanogr.*, *32*(11), 3132-3144.
- Barth, J. A., Fram, J. P., Dever, E. P., Risien, C. M., Wingard, C. E., Collier, R. W., & Kearney, T. D. (2018). Warm blobs, low-oxygen events, and an eclipse: The Ocean Observatories Initiative endurance array captures them all.

- 364 *Oceanography*, 31(1), 90-97. doi: 10.5670/oceanog.2018.114
- 365 Barth, J. A., & Smith, R. L. (1998). Separation of a coastal upwelling jet
366 at cape blanco, oregon, usa. *S. Afr. J. Mar. Sci.*, 19(1), 5-14. doi:
367 10.2989/025776198784126674
- 368 Bethuysen, J., & Thomas, L. N. (2012). Friction and diapycnal mixing at a slope:
369 boundary control of potential vorticity. *J. Phys. Oce.*, 42, 1509-1523. doi: 10
370 .1175/JPO-D-11-0130.1
- 371 Bond, N. A., Cronin, M. F., Freeland, H., & Mantua, N. (2015). Causes and im-
372 pacts of the 2014 warm anomaly in the ne pacific. *Geophys. Res. Lett.*, 42,
373 3414-3420. doi: 10.1002/2015gl063306
- 374 Brink, K. H. (1991). Coastal-trapped waves and wind-driven currents over the con-
375 tinental shelf. *Ann. Rev. Fluid Mech.*, 23, 389-412. doi: 10.1146/annurev.fl.23
376 .010191.002133
- 377 Collins, C. A., Margolina, T., Rago, T. A., & Ivanov, L. (2013). Looping rafos floats
378 in the california current system. *Deep Sea Res. Part II*, 85, 42-61. doi: 10
379 .1016/j.dsr2.2012.07.027
- 380 Connolly, T. P., Hickey, B. M., Shulman, I., & Thomson, R. E. (2014). Coastal
381 trapped waves, alongshore pressure gradients, and the California undercurrent.
382 *J. Phys. Oceanogr.*, 44, 319-342. doi: 10.1175/JPO-D-13-095.1
- 383 Di Lorenzo, E., & Mantua, N. (2016). Multi-year persistence of the 2014/15 North
384 Pacific marine heatwave. *Nature Clim. Change*, 6, 1042-1048. doi: 10.1038/
385 nclimate3082
- 386 Durski, S. M., & Allen, J. S. (2005). Finite-amplitude evolution of instabilities asso-
387 ciated with the coastal upwelling front. *J. Phys. Oceanogr.*, 35(9), 1606-1628.
388 doi: 10.1175/JPO2762.1
- 389 Durski, S. M., Kurapov, A. L., Allen, J. S., Kosro, P. M., Egbert, G. D., Shear-
390 man, R. K., & Barth, J. A. (2015). Coastal ocean variability in the
391 US Pacific Northwest region: seasonal patterns, winter circulation, and
392 the influence of the 2009-2010 El Niño. *Oce Dyn*, 65, 1643-1663. doi:
393 10.1007/s10236-015-0891-1
- 394 Egbert, G. D., & Erofeeva, S. Y. (2002). Efficient inverse modeling of barotropic
395 ocean tides. *J. Atm. Oce. Tech.*, 19(2), 183-204. doi: 10.1175/1520-0426(2002)
396 019(0183:EIMOBO)2.0.CO;2

- 397 Fisher, J. L., Peterson, W. T., & Rykaczewski, R. R. (2015). The impact of
 398 El Niño events on the pelagic food chain in the northern California Cur-
 399 rent. *Global Change Biology, Global Change Biology*(21), 4401–4414. doi:
 400 0.1111/gcb.13054
- 401 Garrett, C., MacCready, P., & Rhines, P. (1993). Boundary mixing and arrested Ek-
 402 man layers: rotating stratified flow near a sloping boundary. *Ann. Rev. Fluid*
 403 *Mech.*, 25, 291–323. doi: 10.1146/annurev.fl.25.010193.001451
- 404 Haine, T. W. N., & Marshall, J. (1998). Gravitational, symmetric, and baroclinic
 405 instability of the ocean mixed layer. *J. Phys. Oceanogr.*, 28(634–658), 634–658.
 406 doi: 10.1175/1520-0485(1998)028<0634:GSABIO>2.0.CO;2
- 407 Hallberg, R., & Rhines, P. B. (2000). Boundary sources of potential vorticity in geo-
 408 physical circulations. In R. M. Kerr & Y. Kimura (Eds.), *Developments in geo-*
 409 *physical turbulence* (p. 51–65). Kluwer.
- 410 Haynes, P. H., & McIntyre, M. E. (1987). On the evolution of vorticity and poten-
 411 tial vorticity in the presence of diabatic heating and frictional or other forces.
 412 *J. Atmos. Sci.*, 44, 828–841.
- 413 Haynes, P. H., & McIntyre, M. E. (1990). On the conservation and impermeability
 414 theorems for potential vorticity. *J. Atmos. Sci.*, 47, 2021–2031.
- 415 Hickey, B. M. (1998). Coastal oceanography of Western North America from the
 416 tip of Baja California to Vancouver Island. In K. H. Brink & A. R. Robinson
 417 (Eds.), *The Sea, Volume 11* (p. 345–393). Wiley and Sons, Inc., New York,
 418 NY.
- 419 Huyer, A. (1983). Coastal upwelling in the California current system. *Prog.*
 420 *Oceanogr.*, 12(3), 259–284. doi: 10.1016/0079-6611(83)90010-1
- 421 Jacox, M. G., Desiree, T., Alexander, M. A., Hervieux, G., & Stock, C. A. (2019).
 422 Predicting the evolution of the 2014–2016 California current system marine
 423 heatwave from an ensemble of coupled global climate forecasts. *Front. Mar.*
 424 *Sci.*, 6, 497. doi: 10.3389/fmars.2019.00497
- 425 Jacox, M. G., Hanzen, E. L., Zaba, K. D., Rudnick, D. L., Edwards, C. A., Moore,
 426 A. M., & Bograd, S. J. (2016). Impacts of the 2015–2016 el niño on the Califor-
 427 nia current system: Early assessment and comparison to past events. *Geophys.*
 428 *Res. Lett.*, 43, 7072–7080. doi: 10.1002/2016GL069716
- 429 Koch, A. O., Kurapov, A. L., & Allen, J. S. (2010). Near-surface dynamics of a

- 430 separated jet in the coastal transition zone off Oregon. *J. Geophys. Res.*, *115*,
431 C08020. doi: 10.1029/2009JC005704
- 432 Kosro, P. M., Huyer, A., Ramp, S. R., Smith, R. L., Chavez, F. P., Cowles, T. J.,
433 ... Small, L. F. (1991). The structure of the transition zone between coastal
434 waters and the open ocean off northern California, winter and spring 1987. *J.*
435 *Geophys. Res.*, *114*(C8), 14707–14730. doi: 10.1029/91JC01210
- 436 Kurapov, A. L., Rudnick, D. L., Cervantes, B. T., & Risien, C. M. (2022). Slope and
437 shelf flow anomalies off Oregon influenced by the remote oceanic mechanism in
438 2014–16. *J. Geophys. Res.: Oceans*. doi: INPRESS
- 439 Kurapov, A. L., Rudnik, D. L., & Pelland, N. A. (2017b). Seasonal and interannual
440 variability in along-slope oceanic properties off the US West Coast: Infer-
441 ences from a high-resolution regional model. *J. Geophys. Res. Oceans*, *122*,
442 5237–5259. doi: 10.1002/2017JC012721
- 443 MacCready, P., & Rhines, P. B. (1991). Buoyant inhibition of Ekman transport on a
444 slope and its effect on stratified spin-up. *J. Fluid Mech.*, *223*, 631–661. doi: 10
445 .1017/S0022112091001581
- 446 MacCready, P., & Rhines, P. B. (1993). Slippery bottom boundary layers on a slope.
447 *J. Phys. Oceanogr.*, *23*, 5–22. doi: 10.1175/1520-0485(1993)023<0005:SBBLOA>
448 2.0.CO;2
- 449 Marshall, J. C., & Nurser, A. J. G. (1992). Fluid dynamics of oceanic thermohaline
450 ventilation. *J. Phys. Oceanogr.*, *22*, 583–595.
- 451 McDowell, S., Rhines, P. B., & Keffer, T. (1982). North Atlantic potential vorticity
452 and its relation to the general circulation. *J. Phys. Oceanogr.*, *12*, 1417–1436.
- 453 McPhaden, M. J. (2015). Playing hide and seek with El Niño. *Nature Clim Change*,
454 *5*, 791–795. doi: <https://doi.org/10.1038/nclimate2775>
- 455 Molemaker, M. J., McWilliams, J. C., & Dewar, W. K. (2015). Submesoscale
456 instability and generation of mesoscale anticyclones near a separation of
457 the California undercurrent. *J. Phys. Oceanogr.*, *45*(3), 613–629. doi:
458 10.1175/JPO-D-13-0225.1
- 459 Moum, J. N., Perlin, A., Klymak, J. M., Levine, M. D., Boyd, T., & Kosro, P. M.
460 (2004). Convectively driven mixing in the bottom boundary layer. *J.*
461 *Phys. Oceanogr.*, *34*(10), 2189–2202. doi: 10.1175/1520-0485(2004)034<2189:
462 CDMITB>2.0.CO;2

- 463 O'Dwyer, J., & Williams, R. G. (1997). The climatological distribution of potential
464 vorticity over the abyssal ocean. *J. Phys. Oceanogr.*, *27*, 2488-2506.
- 465 Pedlosky, J. (1987). *Geophysical fluid dynamics*. Berlin: Springer. doi: 10.1007/978
466 -1-4612-4650-3
- 467 Pelland, N. A., Eriksen, C. C., & Lee, C. M. (2013). Subthermocline eddies over
468 the washington continental slope as observed by seagliders, 2003–09. *J. Phys.*
469 *Oceanogr.*, *43*(10), 2025-2053. doi: 10.1175/JPO-D-12-086.1
- 470 Peterson, W. T., Fisher, J. L., Strub, P. T., Du, X., Risien, C., Peterson, J., &
471 Shaw, C. T. (2017). The pelagic ecosystem in the northern california
472 current off oregon during the 2014–2016 warm anomalies within the con-
473 text of the past 20 years. *J. Geophys. Res. Oceans*, *122*, 7267–7290. doi:
474 10.1002/2017JC012952
- 475 Pierce, S. D., Smith, R. L., Kosro, P. M., Barth, J. A., & Wilson, C. D. (2000).
476 Continuity of the poleward undercurrent along the eastern boundary of
477 the mid-latitude north Pacific. *Deep-Sea Res. II*, *47*(5-6), 811-829. doi:
478 10.1016/S0967-0645(99)00128-9
- 479 Pringle, J. M. (2022). Instabilities in the bottom boundary layer reduce boundary
480 layer arrest and stir boundary layer water into the stratified interior. *J. Geo-*
481 *phys. Res.: Oceans*, *127*, e2021JC017253. doi: 10.1029/2021JC017253
- 482 Risien, C. M., Fewings, M. R., Fisher, J. L., Peterson, J. O., & Morgan, C. A.
483 (2022). Spatially gridded cross-shelf hydrographic sections and monthly clima-
484 tologies from shipboard survey data collected along the Newport Hydrographic
485 Line, 1997–2021. *Data in Brief*, *41*, 107922. doi: 10.1016/j.dib.2022.107922
- 486 Rudnick, D. L., Owens, W. B., Johnston, T. M. S., Karnauskas, K. B., Jakoboski, J.,
487 & Todd, R. E. (2021). The equatorial current system west of the Galápagos Is-
488 lands during the 2014–16 El Niño as observed by underwater gliders. *J. Phys.*
489 *Oceanogr.*, *51*, 3-17. doi: 10.1175/JPO-D-20-0064.1
- 490 Samelson, R. M. (2017). Time-dependent linear theory for the generation of pole-
491 ward undercurrents on eastern boundaries. *J. Physic. Oceanogr.*, *47*(12),
492 3037–3059. doi: 10.1175/JPO-D-17-0077.1
- 493 Thomas, L. N. (2005). Destruction of potential vorticity by winds. *J. Phys.*
494 *Oceanogr.*, *35*, 2457-2466. doi: 10.1175/JPO2830.1
- 495 Williams, R. G., & Roussenov, V. (2003). The role of sloping sidewalls in forming

496 potential vorticity contrasts in the ocean interior. *J. Phys. Oceanogr.*, *33*, 633-
497 648.

498 Zaba, K. D., & Rudnick, D. L. (2016). The 2014–2015 warming anomaly in the
499 southern california current system observed by underwater gliders. *Geophys.*
500 *Res. Lett.*, *43*, 1241-1248. doi: 10.1002/2015GL067550

501 Zaba, K. D., Rudnick, D. L., Cornuelle, B. D., Gopalakrishnan, G., & Mazloff,
502 M. R. (2020). Volume and heat budgets in the coastal California Current
503 system: means, annual cycles, and interannual anomalies of 2014–16. *J. Phys.*
504 *Oceanogr.*, *50*, 1435-1436. doi: 10.1175/JPO-D-19-0271.1

14 **Abstract**

15 Over the continental slope off Oregon at the US West Coast, at 44.6N, vertical strati-
 16 fication is found to be anomalously weak in July-August of 2014 and 2015 both in a re-
 17 gional ocean circulation model and Conductivity-Temperature-Depth (CTD) profile ob-
 18 servations. To understand the responsible mechanism, we focus on the layer between the
 19 isopycnal surfaces $\sigma_\theta = 26.5$ and 26.25 kg m^{-3} that is found between depths 100-300 m
 20 and represents material properties characteristic of the slope poleward undercurrent and
 21 shelf-slope exchange. This layer thickness, about 50 m on average, can be twice as large
 22 during the above-mentioned periods. In the 2009-2018 model analysis, this anomaly is
 23 revealed over the continental slope only in summers 2014 and 2015 and only off the Ore-
 24 gon and Washington coasts (40-47N). The stratification anomaly is explained as the ef-
 25 fect of advection of the seasonal alongslope potential vorticity (PV) gradient by an anoma-
 26 lously strong poleward slope current. In the annual cycle, the zone of strong alongslope
 27 PV gradient is found between 40-47N, supported by the local upwelling that results in
 28 the injection of the large PV in the bottom boundary layer over the shelf followed by its
 29 offshore transport in the slope region. The positive alongslope current anomaly prop-
 30 agates to Oregon with coastally trapped waves as part of the El Niño oceanic response
 31 and can be up to 0.1 m s^{-1} . Advection by this anomalous poleward current results in
 32 transporting the seasonal PV gradient earlier in the season than on average.

33 **Plain Language Summary**

34 Understanding the oceanic dynamics along the continental slopes is important for
 35 understanding material exchanges between the coastal and interior ocean and biologi-
 36 cal diversity. Analysis of a high-resolution, three-dimensional ocean circulation model
 37 helps explain observed variability over the slope. Associated with the global anomaly pat-
 38 tern called El Niño, the along-slope poleward current off Oregon was anomalously strong
 39 in summers 2014 and 2015. This anomalous transport caused alongshore displacement
 40 of the water masses from the south resulting in the vertical spreading of the subsurface
 41 oceanic layers.

42 **1 Introduction**

43 Seasonal ocean variability along the large part of the US West Coast, between Point
 44 Conception and Juan de Fuca Strait (Figure 1), is dominated by strong wind-driven up-

45 welling in summer and downwelling in winter (Huyer, 1983; Hickey, 1998; Austin & Barth,
46 2002; Durski et al., 2015). Upwelling supports an energetic surface intensified southward
47 coastal current, frontal instabilities, eddy generation, and jet separation that contribute
48 to the shelf-interior ocean momentum, heat and material exchange (Kosro et al., 1991;
49 Barth & Smith, 1998; Durski & Allen, 2005; Koch et al., 2010). In June-July each year,
50 a poleward undercurrent develops along the continental slope (Pierce et al., 2000; Collins
51 et al., 2013; Connolly et al., 2014; Molemaker et al., 2015). It is about 25-50 km wide
52 and its core is found between 100-300 m depths. Samelson (2017) explains the under-
53 current as part of the offshore-propagating planetary wave response following the upwelling
54 conditions setup at the coast.

55 Coastal ocean variability in this region is influenced by basin scale oceanic and at-
56 mospheric anomalies. As a recent example, one of the strongest heat waves on the record
57 hit the North-Eastern Pacific (NEP) region in 2014-2016. It was influenced by the emer-
58 gence of the "warm blob" pattern in the Gulf of Alaska early in 2014 followed by a ma-
59 jor El Niño that tried to break through early in 2014, then "fizzled" and reemerged as
60 a major event in 2015 (Bond et al., 2015; McPhaden, 2015; Rudnick et al., 2021; Amaya
61 et al., 2016; Di Lorenzo & Mantua, 2016; Jacox et al., 2016; Peterson et al., 2017; Ja-
62 cox et al., 2019). Kurapov et al. (2022) studied impacts of this El Niño on the coastal
63 ocean dynamics along the US West Coast using a ten-year, 2009-2018, regional ocean
64 model simulation in the domain shown in Fig. 1a. Additional analyses using this model
65 are presented in this paper. The model horizontal resolution is 2 km, which allows it to
66 represent the dynamics driving shelf, slope and interior flows. The model-data compar-
67 isons demonstrate that the model reproduces correctly variability on time scales from
68 several days to seasonal and interannual. In particular, the model reproduces the El Niño
69 major features including the wide-spread warming of the surface layer, coastal sea level
70 rising, and anomalous deepening of the isopycnal surfaces over the slope (Zaba & Rud-
71 nick, 2016; Zaba et al., 2020). In summer 2014 and 2015, the flow over the shelf and slope
72 off Oregon (40-46N) can be explained as a superposition of the seasonal wind-driven up-
73 welling and the El Niño-related downwelling motion that propagates from the southern
74 boundary of the model domain as coastally trapped waves, CTW (Brink, 1991). The upwelling-
75 favorable southward winds in summers 2014 and 2015 are close to average and hence the
76 offshore near-surface transport is close to average. At the same time, the near-bottom
77 cross-shelf current exhibits an offshore anomaly (i.e., the onshore transport is weakened

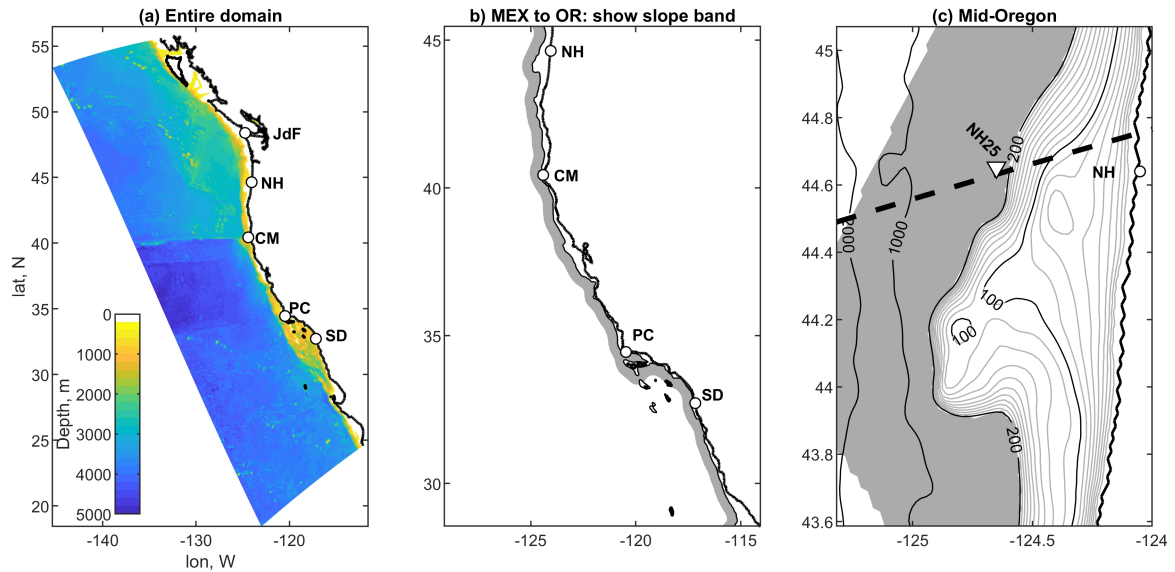


Figure 1. Maps: (a) The entire model domain, color: bathymetry; (b) a close-up on the slope area from Mexico to Oregon, to show the slope band (half-tone), defined as an area 0-40 km offshore of the 200-m isobath (black); (c) a close-up on the mid-Oregon shelf, bathymetric contours are (black) 100, 200, 1000 and 2000 m and (half-tone) from 10 to 190 m every 10 m; NH25 is the location of the ship CTD station and the dashed line is the model section (see Fig. 3 and 6); gray: the slope band. In (a)-(c), circles show geographic reference points: San Diego (SD, 32.7N), Point Conception (PC, 34.4N), Cape Mendocino (CM, 40.4N), Newport, OR (NH, 44.6N), and Juan de Fuca Strait (JdF, 48.4N).

78 or reversed toward offshore). The alongshore current component over the shelf, usually
 79 southward in Oregon, is anomalously weak. Over the slope, the poleward velocity anomaly
 80 adds to the undercurrent. This anomaly is connected to the anomalies near the south-
 81 ern boundary at 24N that propagate all along the slope with the speed of approximately
 82 2.5 m s^{-1} characteristic of CTW.

83 The 10-year model simulation at the 2-km resolution shows very rich behavior over
 84 a wide spectrum of temporal and spatial scales and provides a tool to reveal new anoma-
 85 lies and dynamical effects. In the present study, we utilize the same model solution to
 86 explain episodes of weaker stratification detected over the continental slope off Oregon
 87 in summer 2014 and 2015, both in the model and available observations. This stratifi-
 88 cation anomaly will be explained as the effect of anomalous poleward advection of the

89 seasonal alongslope gradient of the potential vorticity (PV). This will be an example where
90 a local anomaly is forced by a combination of a remote forcing (as the poleward slope
91 current anomaly propagates to the study area with CTW) and a more local, advective
92 mechanism. Explaining this effect will improve our understanding of how the shelf and
93 slope interact.

94 **2 The model and methods**

95 All the model implementation details can be found in (Kurapov et al., 2022) and
96 only a short summary is provided here. The model is based on the Regional Ocean Mod-
97 eling System, ROMS (www.myroms.org), a three-dimensional model describing the non-
98 linear evolution of the stratified ocean. The model domain (Figure 1a) extends along the
99 coast from 24N to 54N, including part of the Mexican coast, all of the US and most of
100 the British Columbia, Canada coasts. The resolution is 2 km in the horizontal and 40
101 terrain-following levels in the vertical direction. The vertical discretization is relatively
102 better near the surface and bottom such that, e.g., the top 50 m are resolved by nine or
103 more layers everywhere; over the shelf, inshore of the 200 m isobath, the bottom 20 m
104 are represented by four or more levels. The vertical coordinate z is directed upward and
105 the mean free surface is near 0; accordingly, the depths of isopycnal surfaces will be re-
106 ported below as $z_\sigma < 0$. Model atmospheric fluxes are computed using ECMWF ERA5
107 fields (ECMWF: European Center for Medium-Range Weather Forecasts, ERA: ECMWF
108 Reanalysis). Non-tidal oceanic boundary conditions are obtained from the HYCOM global
109 US Navy nowcasts (www.hycom.org). The barotropic tidal boundary conditions are added
110 using dominant harmonic constituents from the Pacific regional TPXO estimate (<https://www.tpxo.net/regional>,
111 (Egbert & Erofeeva, 2002)). The model simulation period is 1 October, 2008 – 25 Oc-
112 tober, 2018. Analyses presented below use daily averaged outputs.

113 The model does not assimilate any data inside the domain and provides a contin-
114 uous, dynamically and thermodynamically balanced solution driven only by the atmo-
115 spheric and oceanic boundary fluxes, which is most suitable for process studies.

116 Some of the analyses below are provided for the across-slope-averaged variables.
117 The approximately 40-km wide slope band is defined just offshore of the 200-m isobath
118 (shaded areas in Fig. 1b and c). This band width is chosen to be close to the width of
119 the poleward undercurrent (Pierce et al., 2000). The subsurface alongslope velocity v_s

120 is defined as in (Kurapov et al., 2022) by projecting the horizontal velocity vectors in
 121 cross-slope sections onto the alongslope direction and averaging in the horizontal across
 122 the band and in the vertical between depths of $z = -300$ and -125 m, where the core
 123 of the undercurrent is expected to be found. $v_s(y, t)$ is positive toward the north and is
 124 a function of the alongslope coordinate (precisely, the alongslope distance from the south-
 125 ern boundary) y and time t .

126 The PV is introduced in geophysical fluid dynamics as a dynamical tracer related
 127 to vorticity that is conserved following a fluid element under conditions having no dis-
 128 sipation, mixing or external boundary fluxes. In the most general form (Pedlosky, 1987):

$$PV = \boldsymbol{\omega}_a \cdot \frac{\nabla \lambda}{\rho}, \quad (1)$$

129 where $\boldsymbol{\omega}_a$ is the absolute vorticity vector and $\lambda = \lambda(p, \rho)$, a function of pressure p and
 130 density ρ , is conserved for a fluid element. If $\lambda = \sigma_\theta$ (the potential density), then the
 131 PV flux across the isopycnal surfaces is 0 even in presence of momentum dissipation and
 132 mixing in the ocean interior (Haynes & McIntyre, 1987, 1990). The PV can be injected
 133 in the layer between two isopycnal surfaces only at the atmosphere-ocean interface if the
 134 layer is outcropped (Marshall & Nurser, 1992; Thomas, 2005) or at the sloping ocean
 135 bottom (Hallberg & Rhines, 2000; Williams & Roussenov, 2003; Bethuysen & Thomas,
 136 2012; Pringle, 2022).

137 An approximation to PV adopted in this study will use only the local vertical com-
 138 ponent of the absolute vorticity (Bethuysen & Thomas, 2012):

$$q = (f + \omega)N^2 = (f + \omega) \left(-\frac{g}{\rho_0} \frac{\partial \sigma_\theta}{\partial z} \right), \quad (2)$$

139 where $\omega = \hat{z} \cdot (\nabla \times \mathbf{u})$ is the vertical component of the relative vorticity, \hat{z} the vertical
 140 unit vector, \mathbf{u} the current vector, N the buoyancy frequency, g gravity, and ρ_0 reference
 141 density. In our analyses we will present q (2) on isopycnal surfaces and in the vertical
 142 sections. While the relative vorticity is an important contributor to the PV in the vicini-
 143 ty of the slope boundary (Molemaker et al., 2015), subsurface flows away from the bound-
 144 ary are in nearly geostrophic balance, $\omega/f \ll 1$, at least on the horizontal scales resolved
 145 by our model. To estimate the cross-slope-band averaged, vertically averaged PV between
 146 two selected isopycnal surfaces, specifically $\sigma_\theta = 26.5$ and 26.25 kg m^{-3} , the background

147 PV is used that neglects ω (McDowell et al., 1982; O’Dwyer & Williams, 1997; Kurapov
148 et al., 2017b):

$$q_B = f \frac{g}{\rho_0} \frac{\Delta\sigma_\theta}{\Delta z}, \quad (3)$$

149 where $\Delta\sigma_\theta = 0.25 \text{ kg m}^{-3}$ and $\Delta z = z_{26.25} - z_{26.5}$ is the vertical distance between
150 the selected surfaces. Generally over the slope, $-300 < z_{26.5} < -175 \text{ m}$ and $z_{26.25}$ is
151 found about 50 m above $z_{26.5}$ (Kurapov et al., 2017b). So, over the slope region, the range
152 of depths between $z_{26.5}$ and $z_{26.25}$ is within the limits of -300 and -125 m used in the
153 definition of the alongslope current $v_s(y, t)$.

154 In this paper we will discuss cross-band-slope averaged variables $z_{26.5}(y, t)$, $z_{26.25}(y, t)$,
155 $q_B(y, t)$, and $v_s(y, t)$. To reduce the "noise" due to the slope eddies, a Gaussian filter with
156 the 100-km correlation length scale is applied to these functions in the y direction.

157 Time series analyses involve computation of the annual cycle and anomalies. The
158 annual cycle is defined by fitting the linear combination of the mean and three harmon-
159 ics with the periods of 1, 1/2, and 1/3 year to the time series using the pre-heat-wave
160 years 2009-2013. Kurapov et al. (2022) show that the poleward undercurrent is the salient
161 feature of the $v_s(y, t)$ annual cycle, peaking in Oregon at the end of July with the speed
162 of 0.07 m s^{-1} .

163 To provide observational evidence of episodes of the reduced stratification over the
164 slope off Oregon in the El Niño years, repeated ship CTD profile data are utilized at sta-
165 tion NH25 along the Newport Hydrographic (NH) Line (44.65N) located 25 nautical miles
166 offshore, where the total water depth is $h = 275 \text{ m}$ (Fisher et al., 2015; Peterson et al.,
167 2017; Risien et al., 2022) (Figure 1c). This unique time series, 1999 through present, is
168 a result of the multiyear effort led by W. Peterson, J. Fisher et al. attempting to main-
169 tain the two-week frequency of hydrographic and biogeochemical profile observations at
170 several stations at the NH line, although stations offshore of $h = 200 \text{ m}$ were visited
171 less often.

172 **3 The stratification anomaly over the slope**

173 We have already shown that $z_{26.5}$ over the slope off Oregon is anomalously deep
174 in 2014-2015 (Kurapov et al., 2022). New analyses focus on the anomalies in both $z_{26.5}$

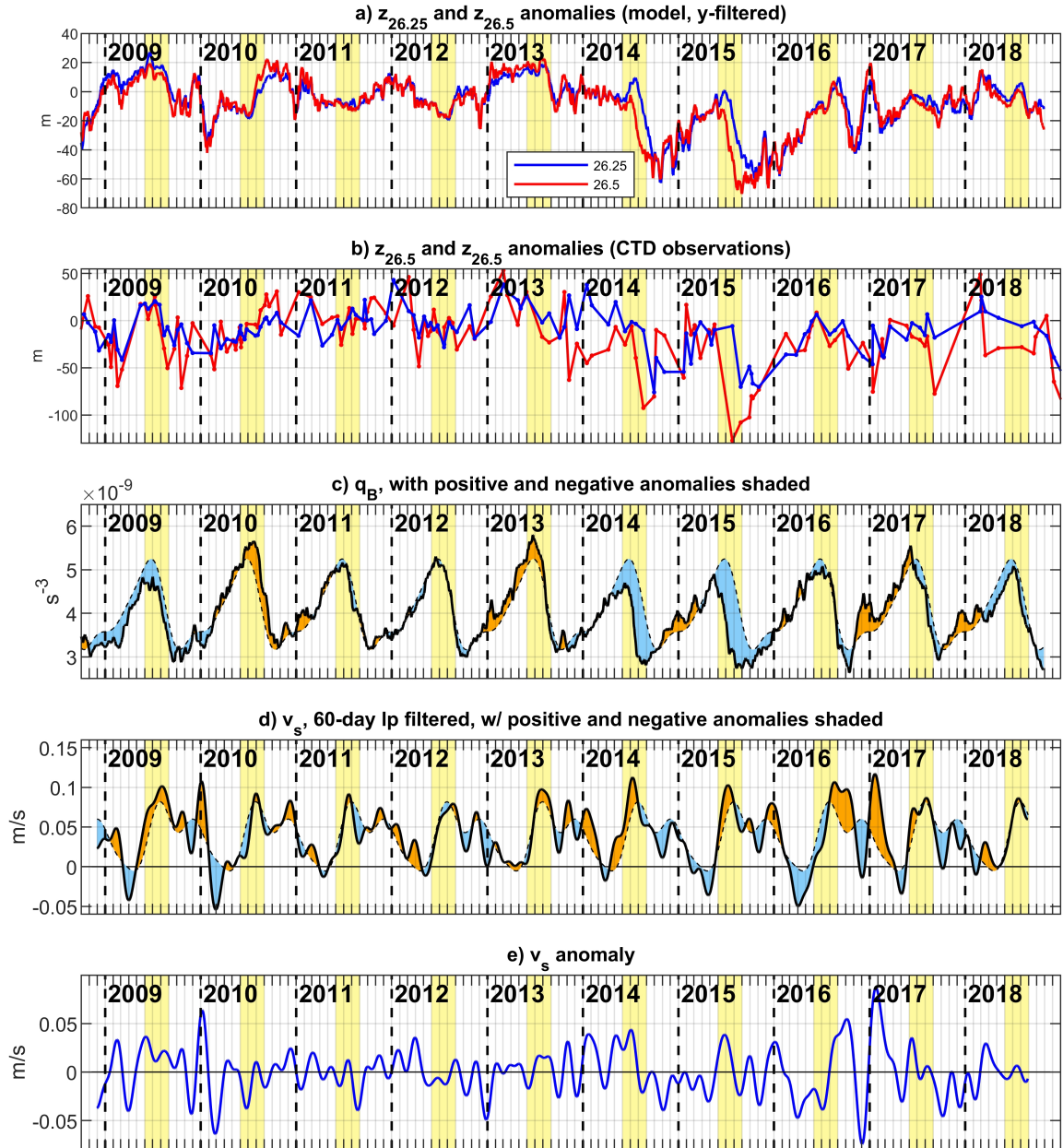


Figure 2. Time series at 44.6N: (a) model $z_{26.5}$ and $z_{26.25}$ anomalies averaged across the slope band (i.e., 0-40 km offshore of the 200-m isobath); (b) observed $z_{26.5}$ and $z_{26.25}$ anomalies, ship CTD at the NH25 station ($h = 275$ m), (c) solid line: model q_B averaged across the slope band, dashed line: annual cycle in q_B ; (d) solid line: v_s , dashed line: annual cycle in v_s ; (e) v_s anomaly. The anomalies are with respect to the annual cycle, based on 2009-2013. In (c) and (d), the orange and blue shades show positive and negative anomalies from the annual cycle. Vertical dashed lines: 1 January of each year. Yellow shades: summer months (JJA). Tick marks on the time axis are on the 1st of each month.

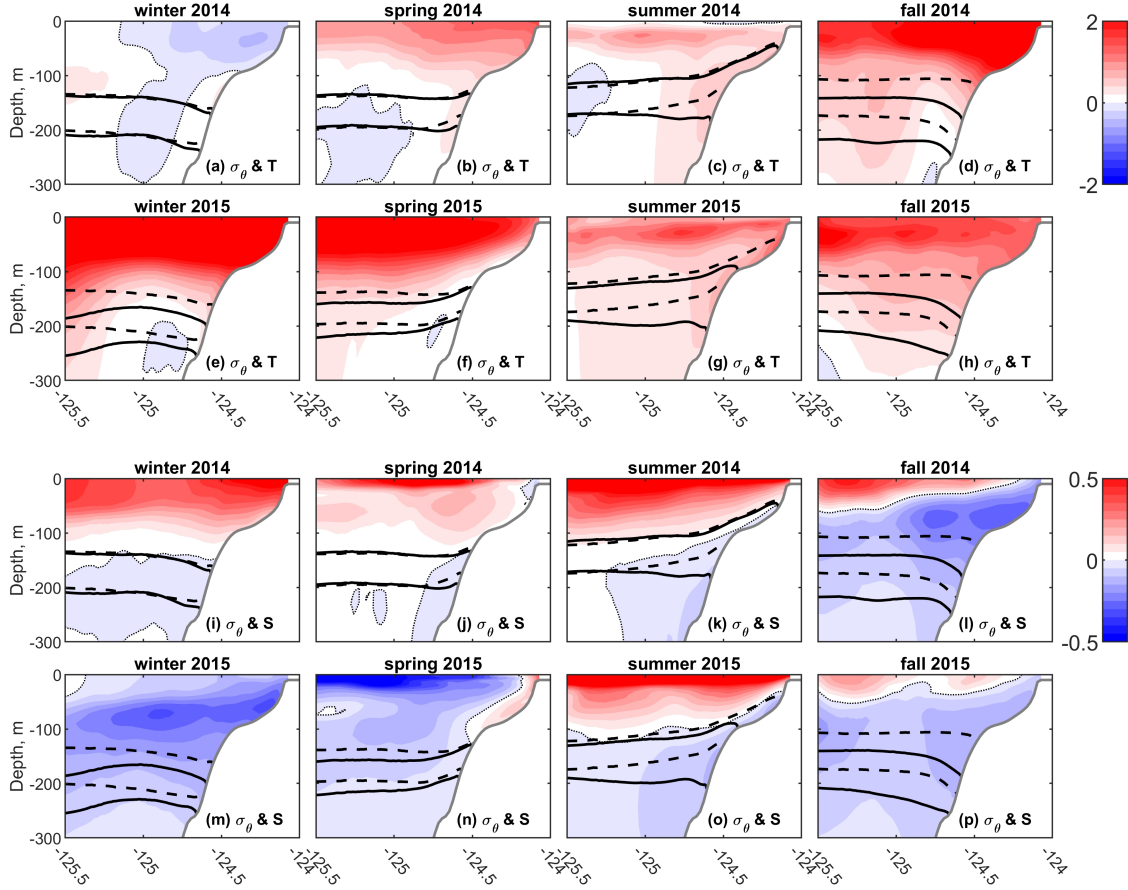


Figure 3. Black thick contours: the seasonally averaged $\sigma_\theta = 26.5$ and 26.25 kg m^{-3} in 2014-2015 in the model cross-shore section near the NH line, 44.6N (see Fig. 1c for the section location): (solid) 3-month averages in 2014 and 2015, (dashed) 2009-2013 average for each season. Background color: seasonal anomalies in (rows 1-2) T ($^\circ\text{C}$), (rows 3-4) S . Winter, spring, summer and fall are defined as DJF, MAM, JJA, and SON, correspondingly. The thin dotted contour shows T or S zero anomaly.

175 and $z_{26.25}$, averaged across the slope band (Figure 2a). These vary in unison (*i.e.*, Δz
 176 anomaly is near 0) for most of the 10-year study period. The notable exceptions are two
 177 periods, July-August of each 2014 and 2015, when not only the depth of each
 178 surface is the deepest, but also Δz is increased by about 50 m. In the NH25 CTD pro-
 179 file data (Fig. 2b), the separation between these layers is also anomalously large during
 180 the same time periods. In 2015, the observed local Δz anomaly is in excess of 100 m.

181 Over the slope off Oregon, q_B averaged between $z_{26.5}$ and $z_{26.25}$ shows a strong up-
 182 welling/downwelling annual cycle (Fig. 2c). The strongest negative anomalies are pre-
 183 sented in summer of each 2014 and 2015, consistent with the strong Δz anomalies dur-
 184 ing the same period. Figure 3 presents this anomaly in a model cross-shore vertical sec-
 185 tion near the NH line (the section location is shown in Fig. 1c). In these section plots,
 186 the thick black contours show 3-month averaged σ_θ in 2014 and 2015 (solid lines) and
 187 seasonal climatological σ_θ (dashed lines). The background color is the seasonal T (rows
 188 1,2) or S anomalies (rows 3,4). Both isopycnal surfaces, 26.25 and 26.5 kg m^{-3} , are near
 189 their climatological levels in winter and spring 2014 (Figure 3a,b,i,j). In summer 2014
 190 (c,k), $z_{26.25}$ is near the climatological level supported by the upwelling favorable winds.
 191 At the same time, $z_{26.5}$ is depressed resulting in the weaker stratification anomaly over
 192 the slope. In fall 2014 (d,l), both isopycnal surfaces are about 50 m below their clima-
 193 tological levels, but the relative distance Δz is again close to the climatology. In win-
 194 ter 2015 (e,m), the isopycnal surfaces are still depressed relative to climatology. By spring
 195 2015 (f,n), these are moved up over the slope by upwelling reaching the climatological
 196 levels over the shelf. Summer 2015 (g,o) is similar to summer 2014 showing the anoma-
 197 lously large spreading between the layers over the slope, mainly due to $z_{26.5}$ anomalous
 198 deepening.

199 In a series of plots in Figure 3a-h, it may be noticed that the $z_{26.5}$ anomaly near
 200 the slope leads the anomaly at the offshore extent of the cross-section shown. This ef-
 201 fect can be associated with the offshore planetary wave propagation (Kurapov et al., 2022).

202 The near-bottom T anomaly over the shelf and slope in summers 2014 and 2015
 203 (Fig. 3c,g) is accompanied by the fresher S anomaly (k,o) and is a signature of the El
 204 Niño-related downwelling. The extreme T anomaly, in excess of 2°C , shows in the top
 205 100 m in fall 2014 (Fig. 3d) after the warm blob waters reach the shelf (Barth et al., 2018).
 206 The strong S anomaly extending over the shelf and slope is evident starting fall 2014.
 207 This and other details of the T and S anomalies are intriguing but require more detailed
 208 analyses and are left as a topic of future studies.

209 To see where along the slope the q_B anomalies reveal themselves and how they may
 210 compare to v_s , the anomalies in $v_s(y, t)$ and $q_B(y, t)$ are shown as Hovmöller diagrams.
 211 Anomalies in v_s (Figure 4a) exhibit fast propagating CTW patterns as discussed in (Kurapov
 212 et al., 2022). In spring-summer 2014 and summer 2015 episodes of sustained positive anoma-

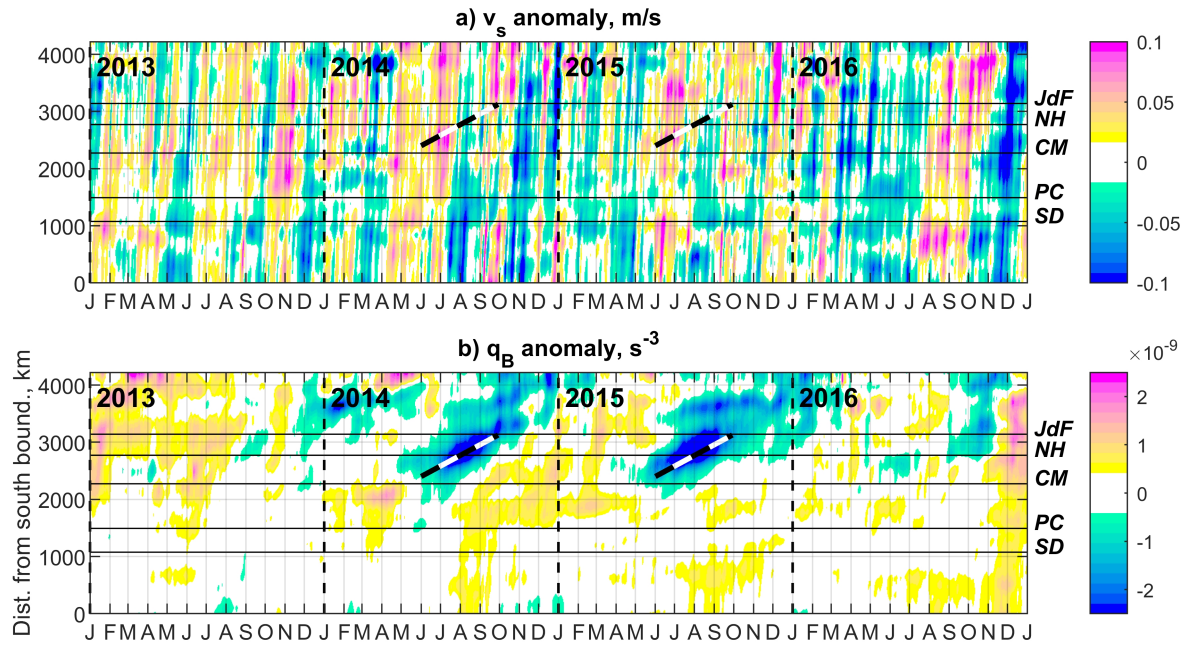


Figure 4. Time vs. alongslope distance plots of anomalies in the slope-band averaged properties, 2013-2016: (a) v_s , (b) q_B . The dashed guidelines correspond to the characteristic advective speed of 0.07 m s^{-1} . Vertical dashed lines show 1 January of each year. Horizontal lines show reference coastal points (see Fig. 1): San Diego (SD, 32.7N), Point Conception (PC, 34.4N), Cape Mendocino (CM, 40.4N), Newport, OR (NH, 44.6N), and Juan de Fuca Strait (JdF, 48.4N).

213 lies reaching 0.1 m s^{-1} are evident, connected to the model southern boundary. In con-
 214 trast, the q_B diagram (Figure 4b) does not show the strong CTW signal. The negative
 215 anomalies of 2014 and 2015 are found only north of Cape Mendocino (CM, 40.4N) in North-
 216 ern California and are the largest between CM and Juan de Fuca Strait (JdF, 48.4N),
 217 i.e. along the coasts of Oregon and Washington. In each summer, the anomalies emerge
 218 just north of CM coinciding with the time of the large positive v_s anomaly. Then the
 219 negative disturbance is transported northward with the speed of 0.07 m s^{-1} character-
 220 istic of the poleward undercurrent.

221 Our hypothesis is that the advection of the alongslope gradient of q by the anoma-
 222 lously strong v_s drives the summer 2014 and 2015 q_B anomalies. In the symbolic form,
 223 the dominant balance is as follows:

$$\frac{\partial q_B}{\partial t} \approx -v_s \frac{\partial q_B}{\partial y}. \quad (4)$$

224 This balance will be tested below (section 5). We already noted in the introduction that
 225 v_s was anomalously strong during those periods. The time series of the total v_s , its an-
 226 nual cycle, and the anomaly at the NH latitude (Figure 2d,e) show that although the
 227 anomalies are not standing out as uniquely large in summer 2014 and 2015, they turn
 228 out to be the largest among all the summers. It is possible that not only the anomaly
 229 magnitude is important but also its longevity and timing relative to the peak of v_s in
 230 the annual cycle. Given the relatively modest speeds at the level of the undercurrent,
 231 to make the alongslope advection in the isopycnal layer a significant contributor to the
 232 tendency in q_B (4), the anomaly in v_s must be accompanied by the strong enough $\partial q_B/\partial y$.

233 4 The seasonal alongslope PV gradient

234 The annual cycle in $q_B(y, t)$ (Figure 5) does indeed show a zone of strong $\partial q_B/\partial y$
 235 that undulates between CM in summer and an area north of JdF in winter. q_B increases
 236 sharply and almost simultaneously in the area between CM-JdF in April, coinciding with
 237 the beginning of the upwelling season. With the onset of the undercurrent in June-July,
 238 the zone of the large gradient starts drifting from CM to JdF with the speed of a few
 239 cm s^{-1} . Notably, the large seasonal gradient $\partial q_B/\partial y$ is found in the same area where
 240 q_B anomalies are detected in 2014 and 2015.

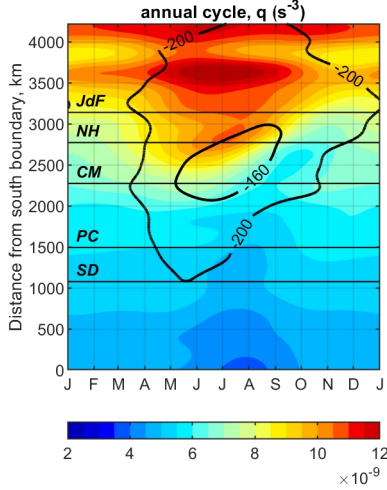


Figure 5. The annual cycle in $q_B(y)$. Black contours: annual cycle in $z_{26.5} = -200, -160$ m. Horizontal lines show reference coastal points (see Fig. 1): San Diego (SD, 32.7N), Point Conception (PC, 34.4N), Cape Mendocino (CM, 40.4N), Newport, OR (NH, 44.6N), and Juan de Fuca Strait (JdF, 48.4N).

241 The reason for the sharply higher q_B in the area of strong upwelling in summers
 242 is found to be due to the PV injection in the bottom boundary layer (BBL) over the slop-
 243 ing shelf bottom (Bethuysen & Thomas, 2012) followed by the PV anomaly entrainment
 244 from the shelf BBL to the interior layer over the slope. Physically, the PV injection across
 245 the sloping bottom during upwelling can be explained first as the geometric effect of the
 246 increase in N the near bottom. Second, the strong tendency toward BBL arrest takes
 247 place (MacCready & Rhines, 1991, 1993; Garrett et al., 1993). As part of this process
 248 the horizontal density gradient established in the BBL due to upwelling is balanced by
 249 the vertical shear in the alongshore velocity component such that the alongshore cur-
 250 rent is reduced near the bottom. As a result, the cross-shore horizontal velocity gradi-
 251 ent is established between points in the BBL and points above the BBL farther offshore
 252 such that $\omega > 0$ near the bottom. So, both N and ω contribute to the increase in q (2)
 253 in the BBL over the sloping bottom.

254 To illustrate that our model represents this process, q is shown together with the
 255 the daily averaged alongslope velocity in the NH cross-shore section (Figure 6). For ex-
 256 ample, on March 31, 2011 (Fig. 6a,c), before the onset of the first upwelling event of the

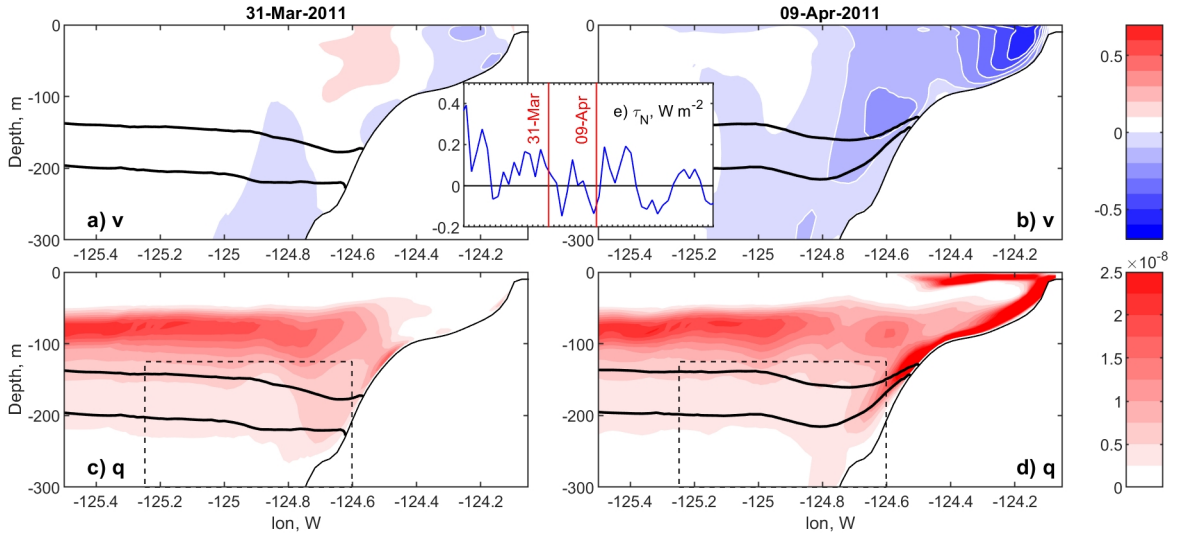


Figure 6. Cross-shore sections near the NH line of daily-averaged (TOP) meridional velocity component, m s^{-1} , (BOTTOM) potential vorticity q , s^{-3} ; (LEFT) 31 March 2011, before the first upwelling event of the year, (RIGHT) 9 April 2011, following the peak of the upwelling event. Black contours are $\sigma_\theta = 26.25$ and 26.5 kg m^{-3} . In (c)-(d), the dashed box is the slope area where v_s average is defined. (e) Daily-averaged meridional wind stress component (northward is positive) between 15 March - 1 May 2011, with red lines showing the dates selected for the cross-section plots.

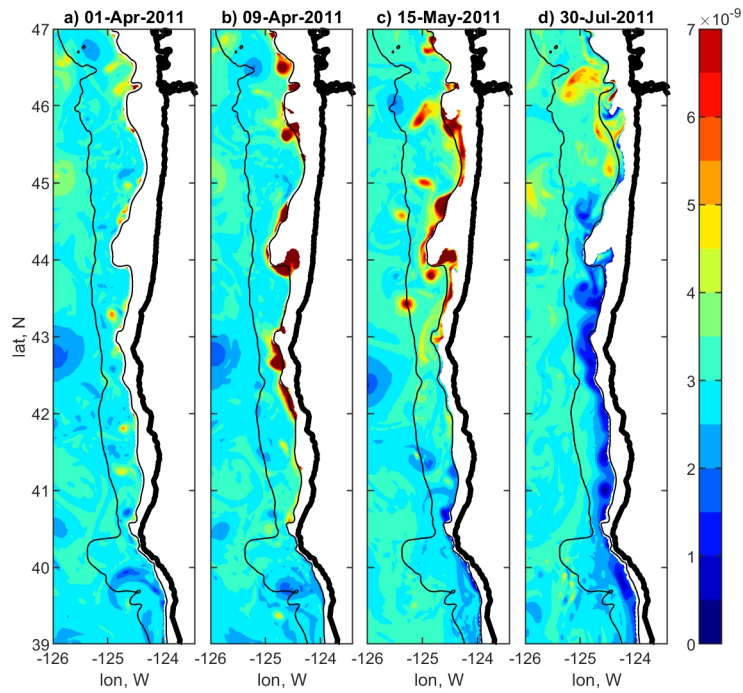


Figure 7. Maps of daily-averaged q (s^{-3}) on the isopycnal surface $\sigma_\theta = 26.5 \text{ kg m}^{-3}$ in the coastal area including Northern CA, all of Oregon and part of Washington State. Black contours are isobaths (200 and 2000 m).

257 year, the alongshelf current is low. At this time, q is relatively large in the interior at
 258 the depth of the winter pycnocline and is low over the shelf. With the onset of upwelling,
 259 as on April 9, 2011 (Fig. 6b,d), q is large over the shelf. In this example, a tongue of high
 260 q is seen in the layer between the surfaces $\sigma_\theta = 26.25$ and 26.5 kg m^{-3} that will be trans-
 261 ported later within that layer to the area over the slope. Maps of the daily-averaged q
 262 computed on $z_{26.5}$ (Figure 7) show relatively low q over the slope before the upwelling
 263 starts (Fig. 7a), followed by episodes of higher q transported with eddies from the shelf
 264 to the slope area following a series of upwelling events (b, c). The emerging undercur-
 265 rent (c,d) is associated with the low q anomaly supported by the negative ω near the slop-
 266 ing bottom (Molemaker et al., 2015). Where the upwelling-related high and undercurrent-
 267 related low q meet, the largest $\partial q/\partial y$ is found. As the season progresses, the undercur-
 268 rent "flushes" the slope waters in Oregon-Washington, pushing the high gradient area
 269 farther and farther north. Note that $\omega < -f$ is a condition for the onset of centrif-
 270 ugal instability (Haine & Marshall, 1998), such that $q > 0$ in Figure 7.

271 Pelland et al. (2013) studied coastal undercurrent eddies, or "cuddies" using glider
 272 hydrographic transects off the coast of Washington. They find that about one third of
 273 the cuddies detected in the ocean interior are anticyclonic and are associated with the
 274 patches of positive PV anomaly. Our model reproduces eddies similar to those anticy-
 275 clonic cuddies (see Fig. 7). The relatively higher PV in these eddies is evidently of the
 276 shelf origin.

277 **5 Term balance analysis for q_B**

278 In this section it will be demonstrated that despite all the approximations that go
 279 into (4), it describes very well the seasonal evolution of the slope averaged q_B as well as
 280 the 2014 and 2015 summer anomalies. To summarize, the approximations include: (i)
 281 ω is neglected; (ii) q_B is the average PV in an area bounded by the two selected isopy-
 282 cnal surfaces and the horizontal extent of the slope band; (iii) v_s is used as the advec-
 283 tive velocity, which is an average in a larger area that includes the selected isopycnal layer
 284 (see the dashed rectangle in Figure 6); (iv) the q flux from the shelf and the slope bot-
 285 tom and the offshore flux are ignored; (v) the alongshore filter is applied to both $v_s(y, t)$
 286 and $q_B(y, t)$; (vi) daily-averaged values are utilized in the model that resolves the tides.
 287 In Figure 8, $TEND = \partial q_B/\partial t$ (half-tone) is compared to $ADV = -v_s \partial q_B/\partial y$ (red) at
 288 the NH latitude; the annual cycle in ADV (blue) is added for reference. $TEND$ is rather

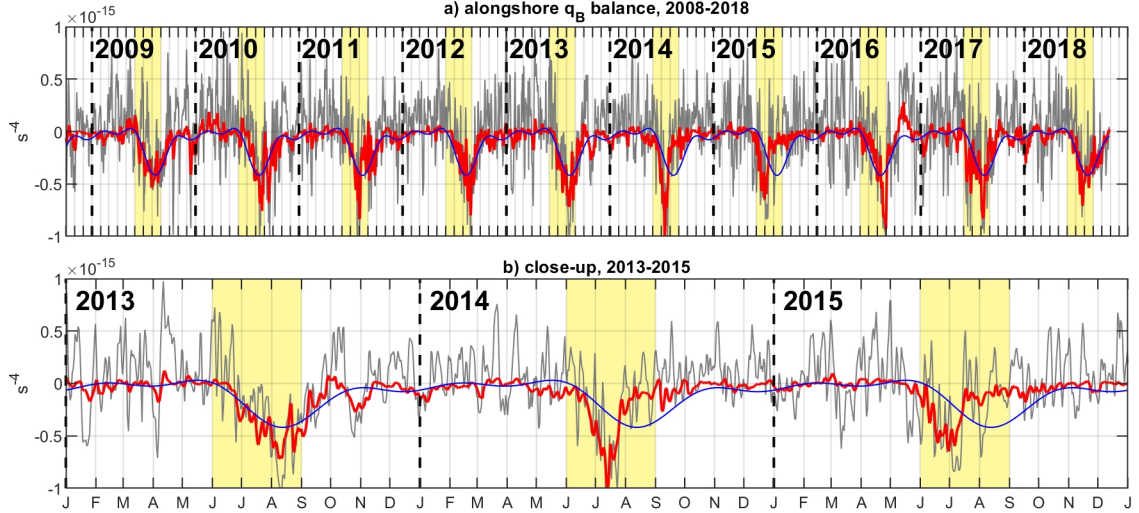


Figure 8. The PV term balance analysis over the slope at NH line: (gray) tendency $\partial q_B/\partial t$, (red) $ADV = -v_s \partial q_B/\partial y$, (blue) annual cycle in ADV (based on 2009-2013). (a) the entire 2008-2018 time period, (b) focus on 2013-2015. Vertical dashed lines: 1 January of each year. Yellow shades: summer months (JJA).

289 noisy as it is estimated from the daily values, but the drop to the strongly negative val-
 290 ues is apparent every summer, associated with the passage of the high $\partial q_B/\partial y$ zone and
 291 the trail of the low q_B in the undercurrent. This pattern is followed very closely by ADV .
 292 In a close-up on 2013-2015 (Figure 8b), it is particularly clear that variability in 2013
 293 is near average, which will be a staple of every year except 2014 and 2015. In those two
 294 years, ADV decreases and recovers about one or two months earlier than on average and
 295 $TEND$ follows the same pattern. It is not necessarily the stronger negative ADV but the
 296 earlier onset of the transition period that makes q_B anomalous in 2014 and 2015.

297 Next, each q_B and v_s can be written as a sum of the annual cycle and anomaly:
 298 $q_B = Q_B + q'_B$ and $v_s = V_s + v'_s$. At the NH location, it is confirmed that $\partial Q_B/\partial t$
 299 closely follows $-V_s \partial Q_B/\partial y$ (not shown). Then,

$$\frac{\partial q'_B}{\partial t} \approx -V_s \frac{\partial q'_B}{\partial y} - v'_s \frac{\partial Q_B}{\partial y} - v'_s \frac{\partial q'_B}{\partial y}. \quad (5)$$

300 The narrative offered so far, that "the slope current anomaly carries the seasonal PV along-
 301 shore gradient" may suggest that the tendency on the lhs of (5) is mostly controlled by

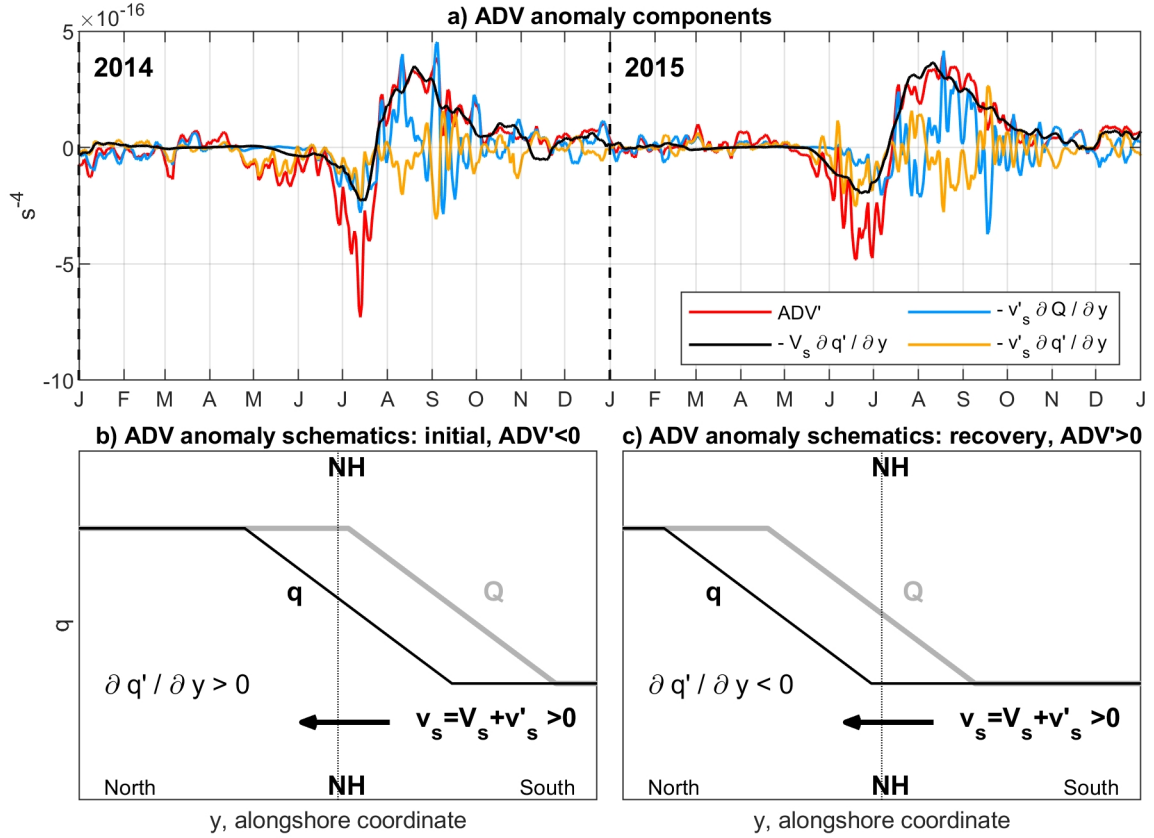


Figure 9. (a) Time series (2014-2015) of the (red) ADV' anomaly and its contributing terms: (black) $-V_s \partial q' / \partial y$, (light blue) $-v'_s \partial Q / \partial y$, (orange) $-v'_s \partial q' / \partial y$; (b-c) schemes explaining the sign of each of the contributing terms to the ADV' anomaly. At the initial phase, all the three contributing terms are negative. At the recovery phase, $\partial q / \partial y$ is small, thus $-v'_s \partial Q / \partial y$ and $-v'_s \partial q' / \partial y$ nearly balance each other.

302 the second term on the rhs. However, this is not the case (Figure 9a). In summer 2014
 303 and 2015, the sum of the all the terms on the rhs of (5), ADV' , goes first through the
 304 initial, negative phase followed by the positive recovery phase. At the initial phase all
 305 the three terms contribute equally to ADV' . At the recovery phase, term $-V_s \partial q'_B / \partial y$
 306 follows closely ADV' and the other two terms on the rhs of (5) nearly balance each other.
 307 This behavior fully supports the assertion that the PV anomalies are caused by the ear-
 308 lier than usual advection of the strong PV front by the anomalously strong current. At
 309 the initial phase (Figure 9b), the zone of the strongest $\partial q / \partial y$ moves through section NH
 310 early, while $\partial Q / \partial y \approx 0$. Hence $\partial q' / \partial y > 0$ and the term $-v'_s \partial q'_B / \partial y$ initiates the neg-
 311 ative anomaly in ADV' . The other two terms will eventually contribute, too, when V_s
 312 and $\partial Q / \partial y$ reach seasonal peaks. At the recovery phase, after the front has passed, $\partial q / \partial y =$
 313 $\partial Q / \partial y + \partial q' / \partial y \approx 0$ such that $-v'_s \partial Q_B / \partial y$ and $-v'_s \partial q'_B / \partial y$ nearly balance each other.

314 **6 Concluding remarks**

315 The regional ocean circulation model helps to discover and explain the events of
 316 anomalous stratification weakening in a layer over the slope off Oregon in July-August
 317 2014 and 2015. The alongslope advection of the strong seasonal PV gradient earlier in
 318 the season than usual explains the PV tendency anomaly and hence the stratification
 319 anomaly. This anomaly is triggered by the anomalously strong (by as much as 0.1 m s^{-1})
 320 and persistent alongslope current anomaly that arrives on the Oregon slope with the coastally
 321 trapped waves originating at the southern boundary and triggered by the El Niño oceanic
 322 mechanism.

323 As part of this study we also evaluated, but could not confirm, if the cross-shore
 324 PV flux anomalies also contribute to the stratification anomalies studied. The expect-
 325 ation was that the downwelling motion associated with the El Niño may provide an ad-
 326 ditional local source of negative PV anomaly over the slope. The downwelling is asso-
 327 ciated with the PV destruction over the slope (Bethuysen & Thomas, 2012) due to the
 328 geometric effect of the weakened stratification near the bottom. Enhanced mixing in-
 329 cluding convective instability (Moum et al., 2004) may also contribute to PV destruc-
 330 tion during downwelling. There is also a possibility that the negative cross-shore veloc-
 331 ity anomaly fluxes this PV deficit into the slope area. However, our analyses of the q flux
 332 across the 200-m isobath at the NH section (not shown) did not exhibit any strikingly
 333 anomalous behavior in the range of depths between $z_{26.5}$ and $z_{26.25}$ in summer 2014 or

2015. Two facts additionally point to the alongslope advection as the dominant mechanism explaining the stratification anomalies: (i) the q_B anomaly is found only where the seasonal $\partial Q/\partial y$ is large, and (ii) this anomaly, first appearing near Cape Mendocino in the Northern CA is displaced to the north with the speed characteristic of the poleward undercurrent.

While surface oceanic processes are well sampled by satellite sensors, subsurface flows remain undersampled. Availability of long-time continuous in-situ observational time series, similar to the CTD set used here, is very important for assessing dynamical processes on intraseasonal, seasonal, and interannual temporal scales. Accurate high-resolution models that show variability consistent with the sparse in-situ data remain important instruments to improve our understanding of subsurface flows, including in our case processes that define the shelf-interior ocean material and heat exchange.

Acknowledgments

We wish to thank Drs. K. Brink, P. MacCready, I. Rivin and J. Pringle for useful discussions. We are grateful to Jennifer Fisher for providing the CTD profile data. This research was partly supported by the NASA grant 80NSSC22K1003.

Data Availability Statement

CTD observations utilized in this study are available as described in (Risien et al., 2022). Model outputs and the entire model setup are freely available upon request to anybody interested in future analyses or developments.

References

- Amaya, D. J., Bond, N. E., Miller, A. J., , & DeFlorio, M. J. (2016). The evolution and known atmospheric forcing mechanisms behind the 2013-2015 north pacific warm anomalies. *US Clivar Var.*, *14*, 1-6.
- Austin, J. A., & Barth, J. A. (2002). Drifter behavior on the Oregon–Washington shelf during downwelling-favorable winds. *J. Phys. Oceanogr.*, *32*(11), 3132-3144.
- Barth, J. A., Fram, J. P., Dever, E. P., Risien, C. M., Wingard, C. E., Collier, R. W., & Kearney, T. D. (2018). Warm blobs, low-oxygen events, and an eclipse: The Ocean Observatories Initiative endurance array captures them all.

- 364 *Oceanography*, 31(1), 90-97. doi: 10.5670/oceanog.2018.114
- 365 Barth, J. A., & Smith, R. L. (1998). Separation of a coastal upwelling jet
366 at cape blanco, oregon, usa. *S. Afr. J. Mar. Sci.*, 19(1), 5-14. doi:
367 10.2989/025776198784126674
- 368 Bethuysen, J., & Thomas, L. N. (2012). Friction and diapycnal mixing at a slope:
369 boundary control of potential vorticity. *J. Phys. Oce.*, 42, 1509-1523. doi: 10
370 .1175/JPO-D-11-0130.1
- 371 Bond, N. A., Cronin, M. F., Freeland, H., & Mantua, N. (2015). Causes and im-
372 pacts of the 2014 warm anomaly in the ne pacific. *Geophys. Res. Lett.*, 42,
373 3414-3420. doi: 10.1002/2015gl063306
- 374 Brink, K. H. (1991). Coastal-trapped waves and wind-driven currents over the con-
375 tinental shelf. *Ann. Rev. Fluid Mech.*, 23, 389-412. doi: 10.1146/annurev.fl.23
376 .010191.002133
- 377 Collins, C. A., Margolina, T., Rago, T. A., & Ivanov, L. (2013). Looping rafos floats
378 in the california current system. *Deep Sea Res. Part II*, 85, 42-61. doi: 10
379 .1016/j.dsr2.2012.07.027
- 380 Connolly, T. P., Hickey, B. M., Shulman, I., & Thomson, R. E. (2014). Coastal
381 trapped waves, alongshore pressure gradients, and the California undercurrent.
382 *J. Phys. Oceanogr.*, 44, 319-342. doi: 10.1175/JPO-D-13-095.1
- 383 Di Lorenzo, E., & Mantua, N. (2016). Multi-year persistence of the 2014/15 North
384 Pacific marine heatwave. *Nature Clim. Change*, 6, 1042-1048. doi: 10.1038/
385 nclimate3082
- 386 Durski, S. M., & Allen, J. S. (2005). Finite-amplitude evolution of instabilities asso-
387 ciated with the coastal upwelling front. *J. Phys. Oceanogr.*, 35(9), 1606-1628.
388 doi: 10.1175/JPO2762.1
- 389 Durski, S. M., Kurapov, A. L., Allen, J. S., Kosro, P. M., Egbert, G. D., Shear-
390 man, R. K., & Barth, J. A. (2015). Coastal ocean variability in the
391 US Pacific Northwest region: seasonal patterns, winter circulation, and
392 the influence of the 2009-2010 El Niño. *Oce Dyn*, 65, 1643-1663. doi:
393 10.1007/s10236-015-0891-1
- 394 Egbert, G. D., & Erofeeva, S. Y. (2002). Efficient inverse modeling of barotropic
395 ocean tides. *J. Atm. Oce. Tech.*, 19(2), 183-204. doi: 10.1175/1520-0426(2002)
396 019(0183:EIMOBO)2.0.CO;2

- 397 Fisher, J. L., Peterson, W. T., & Rykaczewski, R. R. (2015). The impact of
 398 El Niño events on the pelagic food chain in the northern California Cur-
 399 rent. *Global Change Biology, Global Change Biology*(21), 4401–4414. doi:
 400 0.1111/gcb.13054
- 401 Garrett, C., MacCready, P., & Rhines, P. (1993). Boundary mixing and arrested Ek-
 402 man layers: rotating stratified flow near a sloping boundary. *Ann. Rev. Fluid*
 403 *Mech.*, 25, 291–323. doi: 10.1146/annurev.fl.25.010193.001451
- 404 Haine, T. W. N., & Marshall, J. (1998). Gravitational, symmetric, and baroclinic
 405 instability of the ocean mixed layer. *J. Phys. Oceanogr.*, 28(634–658), 634–658.
 406 doi: 10.1175/1520-0485(1998)028<0634:GSABIO>2.0.CO;2
- 407 Hallberg, R., & Rhines, P. B. (2000). Boundary sources of potential vorticity in geo-
 408 physical circulations. In R. M. Kerr & Y. Kimura (Eds.), *Developments in geo-*
 409 *physical turbulence* (p. 51–65). Kluwer.
- 410 Haynes, P. H., & McIntyre, M. E. (1987). On the evolution of vorticity and poten-
 411 tial vorticity in the presence of diabatic heating and frictional or other forces.
 412 *J. Atmos. Sci.*, 44, 828–841.
- 413 Haynes, P. H., & McIntyre, M. E. (1990). On the conservation and impermeability
 414 theorems for potential vorticity. *J. Atmos. Sci.*, 47, 2021–2031.
- 415 Hickey, B. M. (1998). Coastal oceanography of Western North America from the
 416 tip of Baja California to Vancouver Island. In K. H. Brink & A. R. Robinson
 417 (Eds.), *The Sea, Volume 11* (p. 345–393). Wiley and Sons, Inc., New York,
 418 NY.
- 419 Huyer, A. (1983). Coastal upwelling in the California current system. *Prog.*
 420 *Oceanogr.*, 12(3), 259–284. doi: 10.1016/0079-6611(83)90010-1
- 421 Jacox, M. G., Desiree, T., Alexander, M. A., Hervieux, G., & Stock, C. A. (2019).
 422 Predicting the evolution of the 2014–2016 California current system marine
 423 heatwave from an ensemble of coupled global climate forecasts. *Front. Mar.*
 424 *Sci.*, 6, 497. doi: 10.3389/fmars.2019.00497
- 425 Jacox, M. G., Hanzen, E. L., Zaba, K. D., Rudnick, D. L., Edwards, C. A., Moore,
 426 A. M., & Bograd, S. J. (2016). Impacts of the 2015–2016 el niño on the Califor-
 427 nia current system: Early assessment and comparison to past events. *Geophys.*
 428 *Res. Lett.*, 43, 7072–7080. doi: 10.1002/2016GL069716
- 429 Koch, A. O., Kurapov, A. L., & Allen, J. S. (2010). Near-surface dynamics of a

- 430 separated jet in the coastal transition zone off Oregon. *J. Geophys. Res.*, *115*,
 431 C08020. doi: 10.1029/2009JC005704
- 432 Kosro, P. M., Huyer, A., Ramp, S. R., Smith, R. L., Chavez, F. P., Cowles, T. J.,
 433 ... Small, L. F. (1991). The structure of the transition zone between coastal
 434 waters and the open ocean off northern California, winter and spring 1987. *J.*
 435 *Geophys. Res.*, *114*(C8), 14707–14730. doi: 10.1029/91JC01210
- 436 Kurapov, A. L., Rudnick, D. L., Cervantes, B. T., & Risien, C. M. (2022). Slope and
 437 shelf flow anomalies off Oregon influenced by the remote oceanic mechanism in
 438 2014–16. *J. Geophys. Res.: Oceans*. doi: INPRESS
- 439 Kurapov, A. L., Rudnik, D. L., & Pelland, N. A. (2017b). Seasonal and interannual
 440 variability in along-slope oceanic properties off the US West Coast: Infer-
 441 ences from a high-resolution regional model. *J. Geophys. Res. Oceans*, *122*,
 442 5237–5259. doi: 10.1002/2017JC012721
- 443 MacCready, P., & Rhines, P. B. (1991). Buoyant inhibition of Ekman transport on a
 444 slope and its effect on stratified spin-up. *J. Fluid Mech.*, *223*, 631–661. doi: 10
 445 .1017/S0022112091001581
- 446 MacCready, P., & Rhines, P. B. (1993). Slippery bottom boundary layers on a slope.
 447 *J. Phys. Oceanogr.*, *23*, 5–22. doi: 10.1175/1520-0485(1993)023<0005:SBBLOA>
 448 2.0.CO;2
- 449 Marshall, J. C., & Nurser, A. J. G. (1992). Fluid dynamics of oceanic thermohaline
 450 ventilation. *J. Phys. Oceanogr.*, *22*, 583–595.
- 451 McDowell, S., Rhines, P. B., & Keffer, T. (1982). North Atlantic potential vorticity
 452 and its relation to the general circulation. *J. Phys. Oceanogr.*, *12*, 1417–1436.
- 453 McPhaden, M. J. (2015). Playing hide and seek with El Niño. *Nature Clim Change*,
 454 *5*, 791–795. doi: <https://doi.org/10.1038/nclimate2775>
- 455 Molemaker, M. J., McWilliams, J. C., & Dewar, W. K. (2015). Submesoscale
 456 instability and generation of mesoscale anticyclones near a separation of
 457 the California undercurrent. *J. Phys. Oceanogr.*, *45*(3), 613–629. doi:
 458 10.1175/JPO-D-13-0225.1
- 459 Moum, J. N., Perlin, A., Klymak, J. M., Levine, M. D., Boyd, T., & Kosro, P. M.
 460 (2004). Convectively driven mixing in the bottom boundary layer. *J.*
 461 *Phys. Oceanogr.*, *34*(10), 2189–2202. doi: 10.1175/1520-0485(2004)034<2189:
 462 CDMITB>2.0.CO;2

- 463 O'Dwyer, J., & Williams, R. G. (1997). The climatological distribution of potential
464 vorticity over the abyssal ocean. *J. Phys. Oceanogr.*, *27*, 2488-2506.
- 465 Pedlosky, J. (1987). *Geophysical fluid dynamics*. Berlin: Springer. doi: 10.1007/978
466 -1-4612-4650-3
- 467 Pelland, N. A., Eriksen, C. C., & Lee, C. M. (2013). Subthermocline eddies over
468 the washington continental slope as observed by seagliders, 2003–09. *J. Phys.*
469 *Oceanogr.*, *43*(10), 2025-2053. doi: 10.1175/JPO-D-12-086.1
- 470 Peterson, W. T., Fisher, J. L., Strub, P. T., Du, X., Risien, C., Peterson, J., &
471 Shaw, C. T. (2017). The pelagic ecosystem in the northern california
472 current off oregon during the 2014–2016 warm anomalies within the con-
473 text of the past 20 years. *J. Geophys. Res. Oceans*, *122*, 7267–7290. doi:
474 10.1002/2017JC012952
- 475 Pierce, S. D., Smith, R. L., Kosro, P. M., Barth, J. A., & Wilson, C. D. (2000).
476 Continuity of the poleward undercurrent along the eastern boundary of
477 the mid-latitude north Pacific. *Deep-Sea Res. II*, *47*(5-6), 811-829. doi:
478 10.1016/S0967-0645(99)00128-9
- 479 Pringle, J. M. (2022). Instabilities in the bottom boundary layer reduce boundary
480 layer arrest and stir boundary layer water into the stratified interior. *J. Geo-*
481 *phys. Res.: Oceans*, *127*, e2021JC017253. doi: 10.1029/2021JC017253
- 482 Risien, C. M., Fewings, M. R., Fisher, J. L., Peterson, J. O., & Morgan, C. A.
483 (2022). Spatially gridded cross-shelf hydrographic sections and monthly clima-
484 tologies from shipboard survey data collected along the Newport Hydrographic
485 Line, 1997–2021. *Data in Brief*, *41*, 107922. doi: 10.1016/j.dib.2022.107922
- 486 Rudnick, D. L., Owens, W. B., Johnston, T. M. S., Karnauskas, K. B., Jakoboski, J.,
487 & Todd, R. E. (2021). The equatorial current system west of the Galápagos Is-
488 lands during the 2014–16 El Niño as observed by underwater gliders. *J. Phys.*
489 *Oceanogr.*, *51*, 3-17. doi: 10.1175/JPO-D-20-0064.1
- 490 Samelson, R. M. (2017). Time-dependent linear theory for the generation of pole-
491 ward undercurrents on eastern boundaries. *J. Physic. Oceanogr.*, *47*(12),
492 3037–3059. doi: 10.1175/JPO-D-17-0077.1
- 493 Thomas, L. N. (2005). Destruction of potential vorticity by winds. *J. Phys.*
494 *Oceanogr.*, *35*, 2457-2466. doi: 10.1175/JPO2830.1
- 495 Williams, R. G., & Roussenov, V. (2003). The role of sloping sidewalls in forming

496 potential vorticity contrasts in the ocean interior. *J. Phys. Oceanogr.*, *33*, 633-
497 648.

498 Zaba, K. D., & Rudnick, D. L. (2016). The 2014–2015 warming anomaly in the
499 southern california current system observed by underwater gliders. *Geophys.*
500 *Res. Lett.*, *43*, 1241-1248. doi: 10.1002/2015GL067550

501 Zaba, K. D., Rudnick, D. L., Cornuelle, B. D., Gopalakrishnan, G., & Mazloff,
502 M. R. (2020). Volume and heat budgets in the coastal California Current
503 system: means, annual cycles, and interannual anomalies of 2014–16. *J. Phys.*
504 *Oceanogr.*, *50*, 1435-1436. doi: 10.1175/JPO-D-19-0271.1